



Influence of small inertia on Jeffery orbits

Davide Di Giusto, Laurence Bergougnoux, Cristian Marchioli, Élisabeth Guazzelli

► To cite this version:

Davide Di Giusto, Laurence Bergougnoux, Cristian Marchioli, Élisabeth Guazzelli. Influence of small inertia on Jeffery orbits. *Journal of Fluid Mechanics*, 2024, 979, pp.A42. 10.1017/jfm.2023.1007 . hal-04492675

HAL Id: hal-04492675

<https://hal.science/hal-04492675>

Submitted on 6 Mar 2024

HAL is a multi-disciplinary open access archive for the deposit and dissemination of scientific research documents, whether they are published or not. The documents may come from teaching and research institutions in France or abroad, or from public or private research centers.

L'archive ouverte pluridisciplinaire **HAL**, est destinée au dépôt et à la diffusion de documents scientifiques de niveau recherche, publiés ou non, émanant des établissements d'enseignement et de recherche français ou étrangers, des laboratoires publics ou privés.

Banner appropriate to article type will appear here in typeset article

Influence of small inertia on Jeffery orbits

Davide Di Giusto^{1,2†}, Laurence Bergougnoux¹, Cristian Marchioli², and Élisabeth Guazzelli³

¹Aix Marseille Université, CNRS, IUSTI, Marseille, France

²Dipartimento Politecnico di Ingegneria e Architettura, University of Udine, Italy

³Université Paris Cité, CNRS, Matière et Systèmes Complexes UMR 7057, Paris, France

(Received xx; revised xx; accepted xx)

We experimentally investigate the rotational dynamics of neutrally-buoyant axisymmetric particles in a simple shear flow. A custom-built shearing cell and a multi-view shape-reconstruction method are used to obtain direct measurements of the orientation and period of rotation of particles having oblate and prolate shapes (such as spheroids and cylinders) of varying aspect ratios. By systematically changing the viscosity of the fluid, we examine the effect of inertia (which may be originated from either phase) on the dynamical behaviour of these suspended particles up to particle Reynolds number of approximately one. While no significant effect on the period of rotation is found in this small-inertia regime, a systematic drift among several rotations toward limiting stable orbits is observed. Prolate particles are seen to drift towards the tumbling orbit in the plane of shear, whereas oblate particles are driven either to the tumbling or to the vorticity-aligned spinning orbits, depending on their initial orientation. These results are compared to recent small-inertia asymptotic theories, assessing their range of validity, as well as to numerical simulations in the small-inertia regime for both prolate and oblate particles.

Key words: Particle/fluid flow, Suspensions, Slender-body theory

MSC Codes (*Optional*) 76-05, 76T99

1. Introduction

Suspensions of axisymmetrical (or quasi-axisymmetrical) particles are ubiquitous in natural and industrial applications, including plankton dynamics in the ocean (Marchioli *et al.* 2019; Guasto *et al.* 2012), micro-plastic sea-water contamination (Ross *et al.* 2021), red-blood cells dynamics (Goldsmith 1996), paper production processes (Lundell *et al.* 2011), drag reduction in pipelines and naval applications (Hoyt 1972), particle-reinforced composites (Bao *et al.* 1991). A description of these systems is particularly challenging, as their rheology strongly depends on the relative orientation of the particles within the flow. Nevertheless, as long as

[†] Email address for correspondence: digiusto.davide@spes.uniud.it

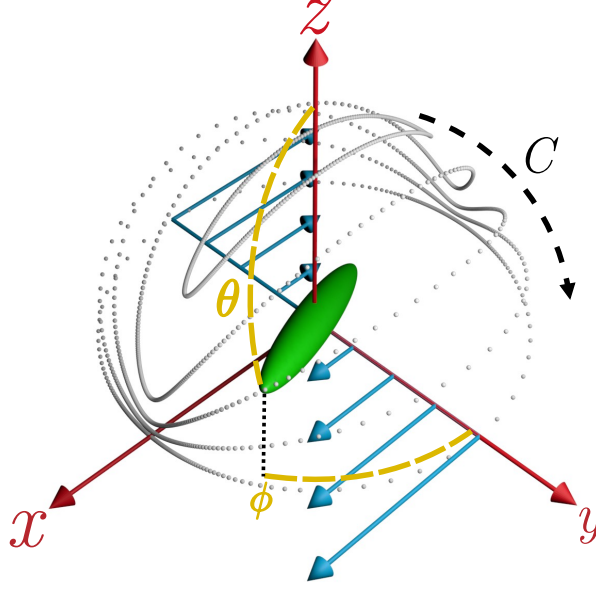


Figure 1: Representation of five different Jeffery orbits for an spheroid of aspect ratio $r = 10$. The azimuthal and polar angles, ϕ and θ , are displayed as yellow dashed lines. The trajectories followed by one of the spheroid extremities are obtained by integrating equation 1.1 in time and displayed as dotted lines on the surface of a sphere of radius equal to the particle half-length ℓ . The orbit constant C increases across the represented orbits following the dashed arrow, from $C = 0$ in the z axis-aligned log-rolling orbit to $C = \infty$ in the tumbling orbit in the x, z plane. See Supplementary Materials for animations.

these particles are shorter than the smallest relevant flow scale, the theory of Jeffery (1922) represents the most common approach to their modelling (Paschkewitz *et al.* 2004; Voth & Soldati 2017; Gustavsson *et al.* 2017).

In the absence of inertial and Brownian forces, Jeffery (1922) found that the axis of revolution of an axisymmetric rigid particle suspended in a simple shear flow rotates along one of an infinite one-parameter family of closed periodic orbits, known as Jeffery orbits, depicted in figure 1. The time change in orientation is given by the equation for the unit vector \mathbf{n} parallel to the axis of revolution:

$$\dot{\mathbf{n}} = \boldsymbol{\Omega} \cdot \mathbf{n} + \frac{r^2 - 1}{r^2 + 1} [\mathbf{E} \cdot \mathbf{n} - \mathbf{n}(\mathbf{n} \cdot \mathbf{E} \cdot \mathbf{n})], \quad (1.1)$$

where $r = \ell/a$ is the particle aspect ratio with ℓ the particle half-length and a its radius. The orientation changes fully with the rate of rotation of the flow, $\boldsymbol{\Omega}$, and only by a fraction $(r^2 - 1)/(r^2 + 1)$ of the rate of strain of the flow, \mathbf{E} . Note that the second term within square parentheses on the right hand side of equation (1.1) is just meant to keep $|\mathbf{n}| = 1$. Considering the uniform shearing motion defined by $(\dot{\gamma}y, 0, 0)$ where $\dot{\gamma}$ is the flow shear rate, the orientation of the particle axis of revolution is described by the azimuthal and polar

angle, ϕ and θ , shown in figure 1. The Jeffery orbits are of the form (with $t = 0$ when $\phi = 0$):

$$\tan \phi = \frac{1}{r} \tan \left[\frac{\dot{\gamma} t}{r + (1/r)} \right], \quad (1.2)$$

$$\tan \theta = \frac{Cr}{(\cos^2 \phi + r^2 \sin^2 \phi)^{1/2}}, \quad (1.3)$$

where the constant of integration C is known as the orbit constant. The period of rotation is $T_J = 2\pi(r + 1/r)/\dot{\gamma}$. The rotational motions consist of infinitely many possible spherical ellipses, limited by a tumbling orbit in the (x, y) plane on the equator of the sphere ($C = \infty$) and a spinning orbit aligned with the vorticity z -axis on the pole of the sphere ($C = 0$).

Since their formulation, many experimental studies have reported Jeffery orbits for spheroids as well as for other axisymmetrical particles such as fibres having $r \gg 1$ and disks having $r \ll 1$ (see e.g. Taylor 1923; Binder 1939; Forgacs & Mason 1959; Goldsmith & Mason 1962a; Karnis *et al.* 1966; Moses *et al.* 2001; Einarsson *et al.* 2016). Interestingly, fibres were observed to rotate with a period comparable to that of spheroids with a lower particle aspect ratio (Trevelyan & Mason 1951). Subsequent experiments with disks (Goldsmith & Mason 1962b) and high-aspect ratio fibres (Anczurowski & Mason 1968) highlighted the shape equivalence existing between spheroidal and cylindrical particles, which could be estimated precisely, moving from a simple linear proportionality (Burgers 1938; Trevelyan & Mason 1951) to a semi-empirical asymptotic theory (Cox 1971), and finally to a data-driven formula (Harris & Pittman 1975). Note that also fore-aft symmetrical particles that possess a discrete rotation symmetry and certain mirror symmetries but do not have a continuous rotation symmetry obey Jeffery's theory, just with different shape parameters, as shown in the seminal paper by Bretherton (1962) and more recently by Fries *et al.* (2017).

In contrast to the case of a suspension of spheres (Einstein 1906, 1911), the first modification to the viscosity of a suspension of spheroids is indeterminate in the limit of the derivation of Jeffery (1922), as the particles exist in a dynamical state depending only on their initial orientation and without steady-state preferential orientation. To solve this indeterminacy, Jeffery himself was the first to suggest that spheroids would eventually align with the local vorticity, driven by the terms neglected in his calculations, namely flow and particle inertia. Taylor (1923) experimentally confirmed this conjecture, whereas different conclusions were later reached by Saffman (1956), who concluded that small particle inertia breaks the Jeffery orbits for nearly spherical particles, showing that log-rolling is stable for nearly spherical prolate particles and unstable for nearly spherical oblate particles. In the following years, few experiments explored the influence of inertia on Jeffery orbits. Preliminary efforts characterised the phenomenon in terms of a slow variation of orbit constant C among consecutive rotations for negligible particle Reynolds number (Goldsmith & Mason 1962b; Stover & Cohen 1990). Karnis *et al.* (1963) found that fibres and disks suspended in circular tubes at particle Reynolds numbers $Re_p \sim 10^{-4}$ would eventually rotate in the tumbling ($C = \infty$) and spinning ($C = 0$) orbits respectively. Yet, to the best of our knowledge, no experimental study has produced a rigorous characterisation of the influence of inertia on the Jeffery orbits.

Instead, weak inertial effects have been thoroughly addressed in a number of theoretical works, from Subramanian & Koch (2005, 2006) and Einarsson *et al.* (2015a,b) to Dabade *et al.* (2016) and Marath & Subramanian (2017, 2018). In particular, Subramanian & Koch (2005) examined the inertial effects on fibre motion in simple shear flow, focusing on the slender-body limit (infinite aspect ratio). In this limit, they were able to derive the fibre orbit equations up to $O(Re)$ where Re is the Reynolds number based on the fibre length. Their

findings were later reproduced both by Einarsson *et al.* (2015a,b) who exploited asymptotic perturbation theory to extend to small shear Reynolds numbers the range of validity of the equation originally proposed by Saffman for spheroidal particles with arbitrary aspect ratio and later by Dabade *et al.* (2016) who also analysed inertial effects in terms of modifications to the Jeffery orbit constant. A common conclusion reached by these independent studies is that the most striking effect of fluid and/or particle inertia is to lift the degeneracy of the infinitely many stable Jeffery orbits. This leads to a drift in the trajectory followed by the particles, which are driven towards a limiting stable orbit through consecutive rotations. Prolate spheroids are only pushed towards the tumbling orbit ($C = \infty$), whereas the situation is more complex for oblate spheroids which are attracted to either the sole spinning orbit ($C = 0$) or both the vorticity-aligned ($C = 0$) and the tumbling ($C = \infty$) orbits, depending on whether their aspect ratio is larger or smaller than a critical value of approximately 0.14 (Einarsson *et al.* 2015b; Dabade *et al.* 2016). Interestingly, Marath & Subramanian (2017) also suggested a second-order effect of inertia on the period of rotation, while Rosén *et al.* (2015) discussed the influence of flow confinement over the stability of the tumbling and spinning orbits.

The problem has been also tackled numerically. Several studies based on the Lattice-Boltzmann method have considered prolate and oblate spheroids in the near-sphere limit (Qi & Luo 2003; Huang *et al.* 2012; Mao & Alexeev 2014). Simulations offer the advantage of easily separating between fluid and particle inertia, characterised by the particle Reynolds number $Re_p = \rho_f \ell^2 \dot{\gamma} / \mu$ and the Stokes number $St = \rho_p \ell^2 \dot{\gamma} / \mu = Re_p \rho_p / \rho_f$, respectively, where ρ_p is the density of the particle, ρ_f that of the fluid, and μ the dynamical viscosity. By exploring a wide parameter space ($0 < Re_p < 300$ and $0 < St < 1200$) for spheroids with moderate aspect ratio $2 \leq r \leq 6$, these authors found a good agreement with the theoretical findings of Dabade *et al.* (2016) and Einarsson *et al.* (2015a) at $Re_p \sim 10$, but also the emerging of other stable rotation states (spinning, inclined spinning, inclined tumbling, or kayaking) for different combinations of increasing particle and flow inertia (Rosén *et al.* 2015). Interestingly, these simulations and previous experiments by Zettner & Yoda (2001) reported an increase of the period of rotation with flow inertia, proportional to $(Re_{p,cr} - Re_p)^{-0.5}$, where $Re_{p,cr}$ is a critical particle Reynolds number above which the considered particles were observed to stop rotating.

In this manuscript, we present the results of an experimental investigation on the rotational dynamics of neutrally-buoyant spheroidal and cylindrical particles (both prolate and oblate) subjected to simple shearing flows in the small-inertia regime ($Re_p = St \lesssim 1$). Since particles and fluid have the same density, we cannot distinguish between specific particle inertia effects and fluid inertia effects. As we will show, however, our findings are valid regardless of the specific phase that is responsible for the observed inertial bias. The experimental methods are described in § 2. The particles and fluids used are described in § 2.1. The custom-built shearing cell is presented in § 2.2. The multi-view shape-reconstruction method used to obtain direct measurements of the particle orientation is introduced in § 2.3 with details of the data processing in § 2.4 and analysis in § 2.5. The experimental results are presented in § 3. Typical evolution of the orbits for both oblate and prolate particles are shown in § 3.1. The period of rotation is examined in § 3.2 where a thorough analysis of the equivalence in shape between spheroids and cylinders is proposed. The drift through successive orbits owing to the effect of inertia is analysed in § 3.3 and compared to the asymptotic theories: first in terms of the time-variation of the particle orientation vector, \mathbf{n} , (Einarsson *et al.* 2015b) and then as the discrete variation of orbit constant, ΔC , against C (Dabade *et al.* 2016). Concluding remarks are drawn in § 4.

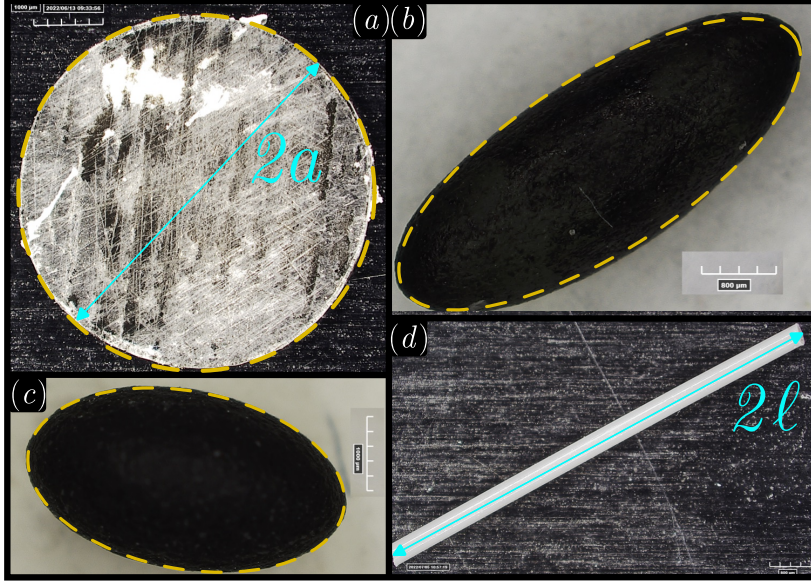


Figure 2: Some typical particles used in the experiments: (a) top view of the disk ‘CYL005’ cut by laser cutter; (b) side view of the spheroidal particle ‘ELL3’; (c) side view of the spheroidal particle ‘ELL06’; (d) side view of the fibre ‘CYL20’ manually cut from fishing line. The yellow dashed curves in panels (a), (b) and (c) represents the circularity of the given ideal shapes.

2. Experimental methods

2.1. Particles and fluids

Some typical cylindrical and spheroidal particles considered in this study are displayed in figure 2. Their shape is determined by taking multiple pictures with a Hirox RH-2000 digital microscope with a resolution of 221 pixels per mm. Then, 10 measurements are manually made using the software ImageJ to produce a statistical characterisation of their length, 2ℓ , and diameter, $2a$, and consequently of their aspect ratio, r , as reported in table 1 where the characteristics of all the particles used are listed. Particles are separated in three different batches according to their production method. The first batch (batch I) comprises two low aspect-ratio fibres (CYL2, CYL10) and all the (oblate and prolate) spheroids. These particles are produced out of UV-sensitive resin using a stereolithography-3D printer with a resolution of $25\ \mu\text{m}$ and have an estimated density of $1200\ \text{kg}/\text{m}^3$. The second batch (batch II) includes two fibres cut from a fishing line and having an estimated density of $1160\ \text{kg}/\text{m}^3$. Finally, the last batch (batch III) contains all the disks obtained by laser cutting of rigid Plexiglas sheets having a density of $1180\ \text{kg}/\text{m}^3$. Cylinders and spheroids coming from batches I and III are further polished using sandpaper after production: for the former, this is done manually to preserve their sharp edges; for the latter, this is undertaken inside a custom sand-paper box shaken at 1000 rpm by a (Hauschild DAC 150.1 FVZ) speed mixer. Since the typical values of the Young modulus E of the three materials is of the order of few gigaPascals, the ratio between viscous and elastic forces $\mathbb{B} = 8\pi\mu\dot{\gamma}\ell^4/(Ea^4\pi/4)$ is vanishingly small ($\mathbb{B} \sim 10^{-5}$) and the particles do not deform within the flow (Du Roure *et al.* 2019).

The fluids used in the experiments are prepared by mixing pure water and citric acid until the solution meets the estimated density of the selected particle. The density of the fluid ρ_f is sampled by means of a highly accurate (Antoon Par) densimeter with an estimated uncertainty of $4\ \text{kg}/\text{m}^3$. Experiments are performed at imposed shear rate $\dot{\gamma}$ and the fluid

Name	Shape	r	ℓ (mm)	a (mm)	κ	Batch
ELL02	Oblate spheroid	0.20 ± 0.01	0.58 ± 0.02	2.91 ± 0.01	0.22 ± 0.01	I
ELL06	Oblate spheroid	0.56 ± 0.01	1.27 ± 0.01	2.28 ± 0.01	0.17 ± 0.01	I
ELL2	Prolate spheroid	1.72 ± 0.02	1.78 ± 0.01	1.04 ± 0.01	0.13 ± 0.01	I
ELL3	Prolate spheroid	2.67 ± 0.06	2.53 ± 0.01	0.95 ± 0.02	0.19 ± 0.01	I
ELL5	Prolate spheroid	5.1 ± 0.1	2.64 ± 0.01	0.52 ± 0.01	0.20 ± 0.01	I
ELL9	Prolate spheroid	9.0 ± 0.1	2.62 ± 0.01	0.29 ± 0.01	0.19 ± 0.01	I
ELL13	Prolate spheroid	13 ± 1	4.7 ± 0.2	0.36 ± 0.02	0.35 ± 0.02	I
CYL005	Disk	0.05 ± 0.01	0.14 ± 0.01	2.58 ± 0.06	0.19 ± 0.09	III
CYL009	Disk	0.10 ± 0.01	0.15 ± 0.02	1.51 ± 0.01	0.11 ± 0.01	III
CYL01	Disk	0.11 ± 0.01	0.31 ± 0.01	2.90 ± 0.04	0.21 ± 0.03	III
CYL02	Disk	0.20 ± 0.01	0.31 ± 0.01	1.56 ± 0.02	0.12 ± 0.01	III
CYL06	Disk	0.56 ± 0.01	1.03 ± 0.01	1.85 ± 0.02	0.14 ± 0.01	III
CYL2	Fibre	1.33 ± 0.02	1.78 ± 0.02	1.34 ± 0.01	0.13 ± 0.01	I
CYL10	Fibre	9.0 ± 0.2	2.59 ± 0.01	0.29 ± 0.01	0.19 ± 0.01	I
CYL15	Fibre	15.4 ± 0.2	3.48 ± 0.01	0.23 ± 0.01	0.26 ± 0.01	II
CYL20	Fibre	20.5 ± 0.7	4.54 ± 0.01	0.22 ± 0.01	0.34 ± 0.01	II

Table 1: Characteristics of all the particles used in the experiments. Columns from left to right: code name, shape, mean aspect ratio r , half-length ℓ , radius a , confinement ratio κ , and identification of the production method.

density is constrained to match that of the particle ($\rho_p = \rho_f$), yielding $Re_p = St$, with Re_p and St defined in § 1. This implies that inertia is mainly controlled by tuning the fluid viscosity μ . This is achieved by adding a certain percentage of Ucon oilTM to the solution, which increases its viscosity from that of pure water up to $\sim 1 Pa \cdot s$ proportionally to its concentration in our experiments, while also slightly decreasing its density.

2.2. Shearing cell

The shearing cell apparatus is displayed in panel (a) of figure 3. It is located in a room at a controlled temperature of $23 \pm 1^\circ C$ and consists of a small tank (500 mm long, 40 mm wide, and 90 mm deep) with 10 mm thick transparent walls on the long sides which has been adapted from the previous work of Metzger & Butler (2012). Two metallic cylinders of diameter 20 mm hang from the lid of the tank and are equipped with polylactic acid (PLA) cylindrical supports that increase their diameter to $L_y = 27$ mm. One is free to rotate and the other is coupled to a transmission shaft through a rolling bearing. A transparent belt is kept under tension between the two cylinders similarly to the photographic roll used in film cameras. It is cut into a rectangular sheet from a 0.1 mm thick flexible MylarTM film and has its extremities kept together by metal staplers. Laser-cut holes in its upper edge enable a gear wheel glued to the rotating cylinder to grip the belt. A rotating motor powered by a DC power supply is connected to the transmission shaft through a drive belt to rotate the gear wheel and drive the transparent belt inside the cell in an infinite loop at constant velocity. The belt is 70 mm tall, extending from nearly the bottom of the shear cell to approximately 15 mm above the free surface.

The fluid within the two parallel sides of the belt is submitted to a confined linear shear where the neutral zero-velocity line lies between the two moving walls. The absolute system of reference is defined as x being the flow direction, y the gradient direction, and z the vorticity direction, parallel to the gravity. In our experiments, the origin is always set at the initial position of the particle placed by hand at the centre of the shear flow. The confinement ratio of the particles is defined as the ratio between the particle length and the distance between the two sides of the transparent belt as $\kappa = 2\ell/L_y$ (Zettner & Yoda 2001). Mean

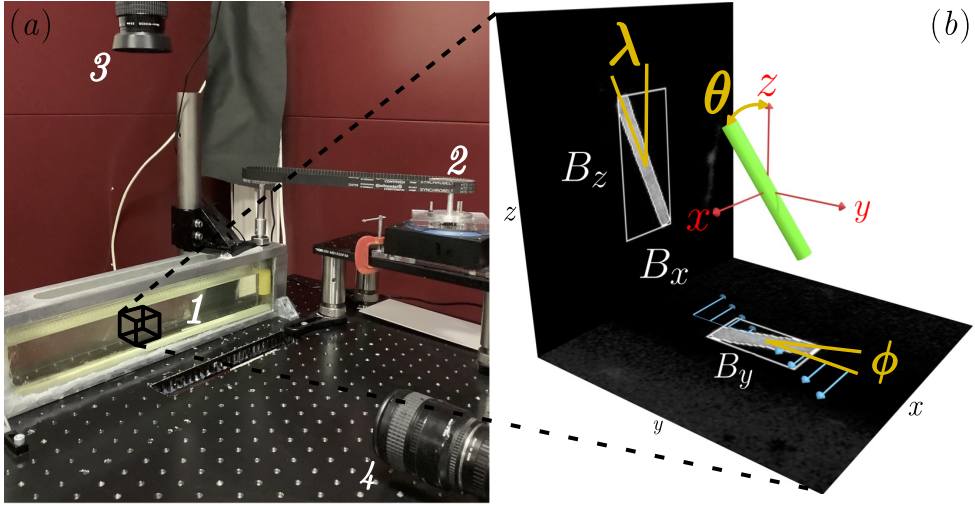


Figure 3: (a) Picture of the experimental setup, where the tank filled with fluid between the two sides of the transparent plastic belt is visible (1), together with the rotating motor and the motion transmission system (2), and the two cameras, looking at the (x, y) flow-gradient plane (3) and at the (x, z) flow-vorticity plane (4). (b) Sketch of the output given by the dual-camera video-recording system. The reference frame is defined at the centre of the particle. The azimuthal and polar angles, ϕ and θ , as well as the projected angle, λ , and the three components of the Axes-Aligned Bounding Box, \mathbf{B} , are also represented. The two recorded frames are displayed on the corresponding flow-gradient and flow-vorticity planes, to appreciate the contrast between the particle projections and the background as well as the detected particle contours and Axes-Aligned Bounding Boxes.

μ (Pa s)	$\dot{\gamma}$ (s^{-1})
0.054 ± 0.001	3.16 ± 0.03
0.400 ± 0.001	3.64 ± 0.05

Table 2: Shear rate measurements for two low and high values of viscosity. Mean values and uncertainties are calculated over 500 velocity fields obtained by Particle Image Velocimetry. The effective shear rates for the other fluids used are obtained by linear interpolation once the fluid characteristics have been finely tuned to match the density of the particles. It is possible to appreciate the small increase of the shear rate $\dot{\gamma}$ with increasing viscosity μ .

values of the confinement ratio are reported in table 1. These values are similar to that considered in the simulations by Rosén *et al.* (2015), namely $\kappa = 0.2$. Based on the results of these simulations, a limited confinement effect on some statistical observables may be expected. This is discussed in more detail in § 3.3 and in § 4.

The shearing flow is examined by shedding light onto three different (x, y) planes at different depths and using Particle Image Velocimetry (PIV). These sections are chosen at least 10 mm below the free surface and above the small unconfined fluid layer laying at the bottom of the cell to characterise a confined region of ~ 30 mm depth where to operate the experiments. The viscosity of the fluid μ is characterised by accurate rheological measurements with an error of 0.001 Pa s on the measurements fully taking into account the real uncertainties. PIV measurements of the shear rate are performed only for two low and

high values of viscosity, reported in table 2. Then, the effective shear rate for each experiment is estimated by linear interpolation between these two measurements, once the fluid properties have been fixed and its density matched to that of the given particle. Secondary circulations are naturally present in such confined flow and can be characterised by finely tuning the parameters of the PIV. They appear to be insignificant when compared to the mean shear. Also, no significant variation of the shear rate is observed across the depth of the region of interest in the shear cell. To summarise, we observe a linear shear rate in a three-dimensional region the sizes of which are determined by the width of the camera field in the flow direction ($L_x = 140$ mm), by the distance between the two inner sides of the transparent plastic belt in the gradient direction ($L_y = 27$ mm) and by the depth of the different PIV measurements in the vorticity direction ($L_z = 30$ mm).

2.3. Measurements

A multi-view video recording system is deployed in the experiments, as shown in panel (b) of figure 3. Jeffery orbits are three-dimensional, but given the axisymmetric nature of the particles, the number of variables that specify the orientation reduces to two. Therefore, measurements of the particle spin were not performed. The objective of this multi-view system is to provide a three dimensional reconstruction of the orientation of each particle given by its direction vector \mathbf{n} . Whereas three or more particle projections would permit a direct resolution (Eberly 1999), we are limited to two complementary images of the axisymmetric particle which are post-processed to reconstruct the orientation as explained in § 2.4.

The cameras are two Allied Prosilica GX1910 cameras, with a resolution of 1920×1080 pixels. Both cameras are equipped with a Nikon Micro-Nikkor 55 mm f2.8 objective, imaging the shear cell from a distance of approximately half a meter with a resolution of 20 pixels per mm. As they have their axes perpendicular, these cameras provide two complementary images: one of the flow-vorticity plane and the other of the flow-gradient plane, as seen in figure 3(a). Considering that the depth of field is enhanced to an estimated value of 3 cm, we verified that distortion and diffraction phenomena are negligible by measuring a check-board patterned object in the flow volume of interest inside the shear cell. The two cameras are controlled by an in-house developed Matlab script.

Experiments are performed as follows. After having filled the cell with the density matched fluid and started shearing, a single particle is manually positioned at the centre of the camera fields, as close as possible to the neutral plane in the middle of the shearing flow. The particle is pre-sheared for a short time to avoid any influence of the positioning operation on its dynamics. Note that, when repeated, this positioning method results in randomly-varying initial orientations despite all the care that can be taken. Then, the recording of the two videos is started and the cameras are synchronised by a manually activated light signal. The recording is stopped before the particle leaves the camera fields. Experiments are typically repeated between 5 and 10 times for a given particle at each particle Reynolds number, as reported in table 3. Typically, at least two complete periods of rotation must be observed in order to validate the run. This requirement happened to be rather challenging for the most slender particles.

2.4. Image processing

Each recorded video is processed by an in-house developed Python script based on the Canny method (Canny 1986), implemented using the OpenCV library (Bradski 2000). The script performs a simple detection routine based on the contrast between the background and the object to be detected. After having reduced the camera field to a small square section of size

Particle	$Re_p, n_{runs}, \overline{\Delta t_{run}}/T$							
ELL02	0.040, 5, 6.06	0.05, 5, 2.77						
ELL06	0.010, 5, 8.40	0.02, 5, 6.90	0.03, 5, 4.62	0.44, 11, 6.46	1.04, 6, 9.71			
ELL2	0.003, 5, 5.49 0.120, 10, 8.65	0.006, 5, 6.39 0.132, 10, 3.22	0.023, 5, 3.09 0.329, 10, 5.75	0.038, 5, 16.17 0.375, 4, 11.07	0.042, 5, 4.06	0.073, 10, 3.37	0.085, 8, 13.28	
ELL3	0.544, 7, 7.20	1.300, 6, 5.31						
ELL5	0.008, 5, 1.68	0.014, 5, 2.63	0.051, 5, 2.69	0.092, 5, 2.04	0.161, 10, 1.74	0.291, 10, 1.67		
ELL9	0.007, 5, 2.63	0.010, 5, 2.07	0.048, 10, 2.16	0.088, 10, 1.70	0.158, 6, 1.73	0.286, 5, 2.03	0.642, 9, 3.63	
ELL13	0.180, 5, 2.00							
CYL005	0.032, 5, 2.15	0.100, 10, 2.65	0.236, 10, 2.20	0.247, 10, 2.72	0.347, 11, 2.53	0.778, 10, 2.44		
CYL009	0.011, 5, 2.54	0.088, 10, 5.12	0.195, 11, 2.84	0.344, 10, 3.40				
CYL01	0.042, 5, 3.57	0.074, 5, 3.22	0.336, 10, 4.99	1.318, 10, 3.42				
CYL02	0.005, 5, 3.73	0.009, 5, 6.16						
CYL06	0.039, 10, 8.27	0.246, 10, 12.85						
CYL2	0.002, 5, 5.51	0.005, 10, 6.48	0.033, 10, 4.23	0.059, 10, 6.98	0.187, 10, 4.31	0.336, 5, 7.57		
CYL9	0.007, 5, 2.51 0.180, 13, 3.24 0.790, 10, 3.53	0.013, 5, 2.28 0.230, 5, 1.39 0.986, 14, 2.85	0.047, 5, 2.03 0.250, 10, 2.52	0.080, 10, 5.33 0.260, 11, 2.82	0.085, 5, 2.12 0.410, 10, 1.73	0.100, 10, 3.98 0.480, 10, 3.78	0.150, 10, 4.39 0.510, 15, 3.03	
CYL15	0.059, 5, 2.08							
CYL20	0.100, 5, 1.89							

Table 3: For each particle type used in the experiments (first column), the particle Reynolds number, Re_p , the number of runs, n_{runs} , and the mean duration of the shearing normalized by the (experimentally measured) mean period of rotation, $\overline{\Delta t_{run}}/T$, are provided.

252 $4 \max(\ell, a) \times 4 \max(\ell, a)$ around the particle, a Gaussian blur and manual threshold filters
 253 are applied to reduce the noise and improve the contrast by smoothing out possible defects
 254 of the transparent plastic belt. At this point, there is a strong intensity gradient between the
 255 particle and the background. Identifying this gradient using the Canny edge filter provides
 256 the closed contour of the given particle. A least-squared optimisation method yields the
 257 orientation angle (fitEllipse function of the OpenCv library), while the extent of the contour
 258 in the aligned directions leads to the estimation of its minimum two-dimensional Axis-
 259 Aligned Bounding Box (boundingRect function of the OpenCv library). By Axis-Aligned
 260 Bounding Box (AABB hereinafter), we mean the smallest rectangle (parallelepiped when
 261 generalising to three dimensions) that is tangent to the particle projection (particle in three
 262 dimensions). The three measurements are stored and the script analyses the videos frame by
 263 frame. The accuracy of the proposed particle detection method has been evaluated against
 264 8100 virtual images of randomly oriented disks and fibres, with a resolution of 7 pixels over

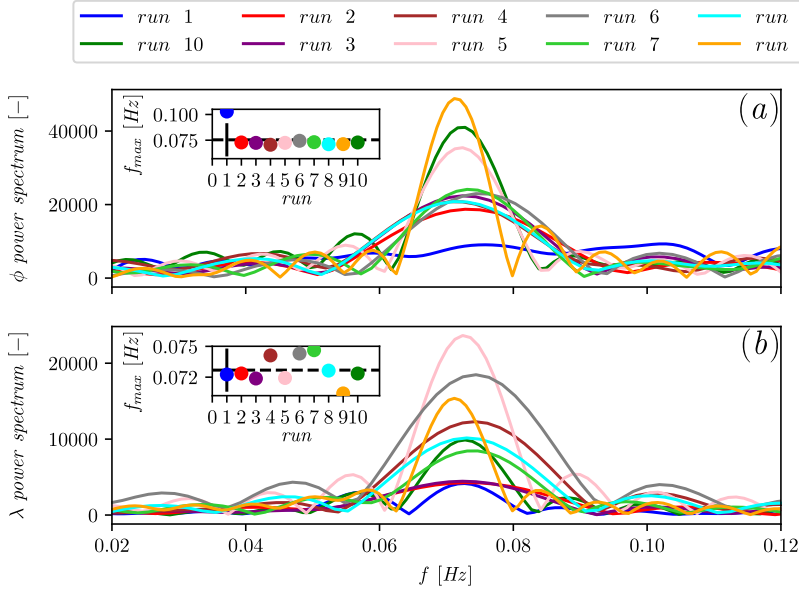


Figure 4: Power spectra of the two projected angles (a) ϕ and (b) λ , for 10 different experimental runs for the fibre CYL10 of aspect ratio $r = 9$ at $Re_p = 0.08$. The insets in each panel show the maximum peak frequency versus the considered runs.

the smallest particle dimension. We found that the Euclidean norm error between theoretical and measured AABBs is below 4 pixels, while the absolute error on the measured angle rarely reached a value above 2° .

Two lists of positions, orientations, and AABB components of the particle projections onto the flow-gradient and in the flow-vorticity planes in time are the result of the post-processing of each experiment made by the Python script. Then, by a suitable re-scaling, it is possible to combine the information collected by the two cameras and produce three-dimensional measurements of the translation and rotation of the particles. The procedure is non-trivial for the estimation of the orientation of each particle because, as displayed in figure 3, while the particle projection in the (x, y) plane provides the azimuthal angle ϕ , the projection in the (x, z) plane determines the angle λ , which only corresponds to θ in the flow-aligned positions. Therefore, given the possibility of producing long lists of three-dimensional AABBs by knowing the particle orientation vector, we choose a data-driven method to regress the orientation of the particle by a two-camera view system. As detailed in Appendix A, we deploy a simple Deep Learning model, implemented using Tensorflow and trained over synthetic data, to perform a three-variable regression and estimate the particle orientation vector \mathbf{n} from the experimentally measured three-dimensional AABBs.

2.5. Data analysis

The data processing of § 2.4 provides the orientation of the axisymmetric particle. This is the key information needed when constructing the Jeffery orbits, discussed in § 3.1, and obtaining the time evolution of the three components of \mathbf{n} , discussed in § 3.3. There are two other important quantities: The period of rotation and the orbit constant, described below and used in § 3.2 and § 3.3, respectively.

Since experimental runs can last up to several particle rotations, the measured projected angles, ϕ and λ , can be interpreted as time series and characterised by Fourier analysis. The Fourier transform of the angular signals can be computed. As a typical example, the

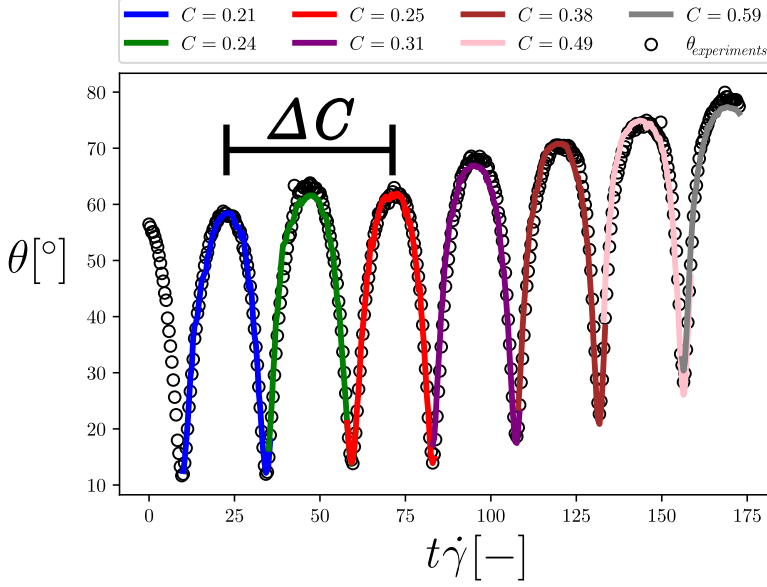


Figure 5: Time-evolution of the reconstructed angle $\theta = \arccos n_3$ (black circles). The fitted forms of equation (1.3) are also plotted as solid lines. The different colours correspond to the estimated values of the orbit constant C reported in the legend. The quantity ΔC represents the variation of the orbit constant in each of the measurements.

power spectra of ten experimental runs are plotted against the frequency in figure 4 for the fibre CYL10. This figure shows that the signal power is coherently resonating around a characteristic frequency, calculated as the frequency f_{max} of the peak of each power spectrum. The period of rotation of the given particle, T , is then estimated as the inverse of this frequency. Measurements are then collected over several runs for a sound statistical characterisation, choosing between the angles ϕ and λ according to a minimum squared error criterion. Averages are computed and uncertainties are estimated as standard deviations over all the experimental runs at a given Re_p .

The components of the reconstructed particle orientation vector \mathbf{n} can provide the azimuthal and polar angles, defined as:

$$n_1 = \sin(\phi) \sin(\theta), \quad (2.1)$$

$$n_2 = \cos(\phi) \sin(\theta), \quad (2.2)$$

$$n_3 = \cos(\theta). \quad (2.3)$$

Equation (1.3) can then be fitted over the reconstructed values of ϕ and θ to estimate the orbit constant C of the given Jeffery orbits, as displayed in figure 5. This is done by a non-linear least squares minimisation (curvefit function of the Scipy Python library) over an observation window manually centred around each flow-aligned position and with total width comparable to half the period of rotation, producing two separate orbit constant measurements for each Jeffery orbit. Orbit constant variations ΔC are then calculated as discrete differences over one period of rotation. This choice is motivated by a classical approach to the analysis of periodic dynamical systems (Glendinning 1994), according to which the flow of the orbit constant C is obtained by its discrete variations between flow-aligned positions over one period T . Recalling the orbit coordinates τ and C introduced by Leal & Hinch (1971), this is equivalent to dropping the temporal dependency of the system (τ) and focusing only on the evolution of its phase (C), similarly to what done in Dabade *et al.* (2016). Therefore, the

intensity of the orbit variation ΔC has a sign indicating the direction of the orbit constant motion, i.e. positive when towards the tumbling orbit ($C = \infty$) and negative when towards the spinning orbit ($C = 0$), and a value the magnitude of which quantifies the stability of a given Jeffery orbit (more unstable orbits will experience stronger variations).

3. Experimental results

3.1. Jeffery orbits

Typical experimental Jeffery orbits for a fibre of aspect ratio $r = 9$, for an oblate spheroid of aspect ratio $r = 0.6$, and for the disk of aspect ratio $r = 0.1$ are shown in figure 6 (a),(b) and (c),(d) and (e),(f) respectively. The coloured dots represent the intersection of the axis given by the orientation vector \mathbf{n} with the half sphere of radius ℓ for the prolate particles and a for the oblate particles, respectively. The location of the intersection was captured during three different experimental runs for each panel and reconstructed as detailed in § 2.4. The corresponding Jeffery orbits at zero inertia are also displayed as solid black lines. They were obtained by integration of equation (1.1) using the first flow-aligned orientation of each experimental run as initial condition.

At low inertia, i.e. for the fibre of panel (a) at $Re_p = 0.08$, the spheroid of panel (c) at $Re_p = 0.02$, and the disk of panel (e) at $Re_p = 0.05$, there is no significant change between the successive rotations for runs with different initial conditions, i.e. different orbit constants. The experimental orbits are in good agreement with the theoretical Jeffery orbits, represented by the black spherical ellipses.

As inertia becomes finite, i.e. for the fibre of panel (b) at $Re_p = 1$, the spheroid of panel (d) at $Re_p = 0.43$, and the disk of panel (f) at $Re_p = 1.32$, the picture slightly changes. The experimental orbits are still spherical ellipses, but they depart from the zero-inertia orbits as their shapes evolve between successive rotations.

For the fibre of panel (b), the orbits are expanding towards the tumbling orbit ($C = \infty$) on the equator of the sphere, i.e. in the (x, y) flow-gradient plane. It is worth mentioning that the orbits are not equally unstable as the fibre experiences a stronger drift when describing intermediate orbits (run 13) than when close to the rolling (run 14) and tumbling (run 3) cycles.

The oblate particles are also drifting through consecutive orbits, but their behaviour is more complex as two limiting stable orbits exist. As shown in panel (d), the spheroid can either drift to a tumbling orbit ($C = \infty$) in the plane of shear (run 10) or to a spinning orbit ($C = 0$), i.e. aligning its orientation vector with the direction of vorticity, z (runs 5 and 8). It is interesting to note that the two orbits closer to the pole of the half sphere (runs 5 and 8) are attracted toward the spinning orbit ($C = 0$) while the other orbit, which is starting with a much larger orbit constant (run 10), is drawn toward the tumbling orbit ($C = \infty$) on the equator of the half sphere. A similar description holds for the disk of panel (f), which exhibits both consecutive rotations in the tumbling orbit ($C = \infty$, run 2) and a systematic drift towards the spinning orbit ($C = 0$, runs 1 and 9).

A comment is in order regarding the separation between consecutive rotations, which appears larger for the more slender particles, i.e. the fibre with $r = 9$ of panel (b) and the disk with $r = 0.1$ of panel (f), than in the case of the spheroid with $r = 0.6$ of panel (d).

3.2. Period of rotation

The dimensionless period of rotation, $T\dot{\gamma}/2\pi$, of the axisymmetric particles is displayed against particle aspect ratio, r , in figure 7. The main panel (a) shows all the results obtained for both prolate and oblate particles, while the two smaller panels distinguish between (b)

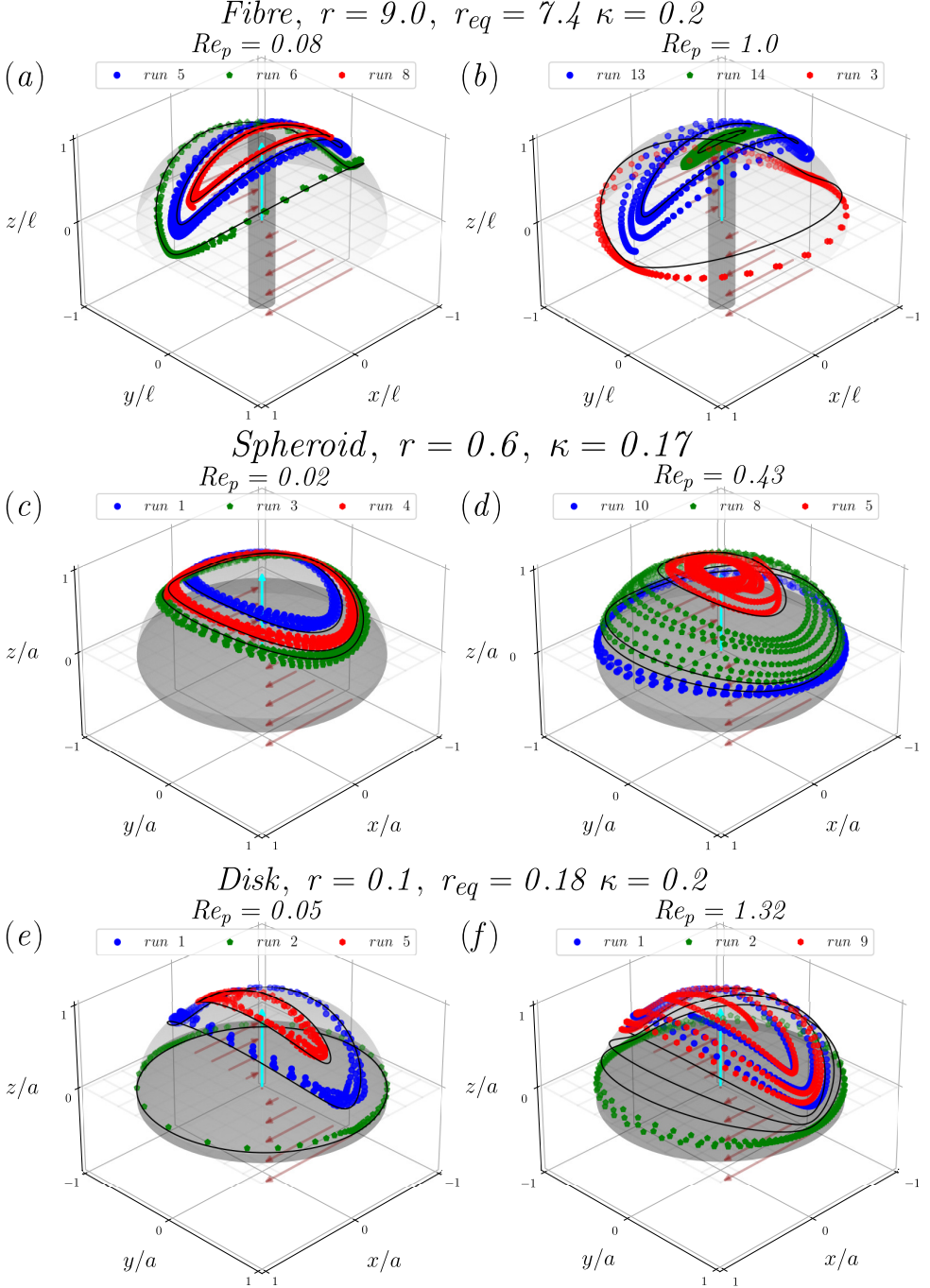


Figure 6: Experimental Jeffery orbits at two Reynolds numbers for the fibre CYL10 (top-row panels), the spheroid ELL06 (middle-row panels) and the disk CYL01 (bottom-row panels): (a) Fibre, $r = 9.0$, $Re_p = 0.08$; (b) Fibre, $r = 9.0$, $Re_p = 1.0$; (c) Spheroid, $r = 0.6$, $Re_p = 0.02$; (d) Spheroid, $r = 0.6$, $Re_p = 0.43$; (e) Disk, $r = 0.1$, $Re_p = 0.05$; (f) Disk, $r = 0.1$, $Re_p = 1.32$. The particles considered in this figure are shown in the vorticity-aligned position with their orientation vector \mathbf{n} highlighted in cyan. The coloured dots represent the intersections of the axis given by the orientation vector \mathbf{n} with the half sphere of radius ℓ for the prolate particles and a for the oblate particles, respectively. The corresponding Jeffery orbits are also displayed as solid black lines and were obtained by integrating equation (1.1) from an initial condition given by the first flow-aligned orientation of each experiment. See Supplementary Materials for animations.

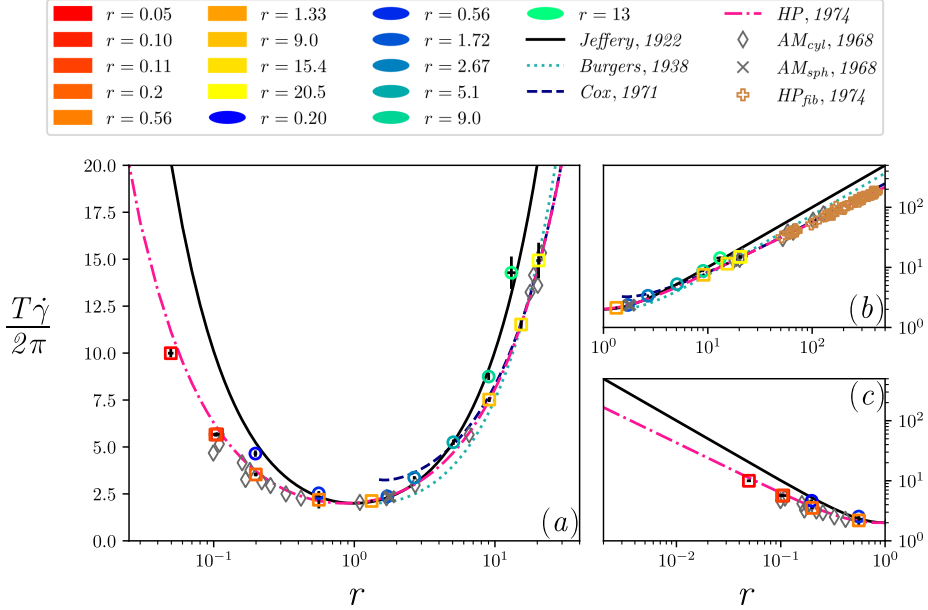


Figure 7: Period of rotation, T , of the axisymmetrical particles against the particle aspect ratio r . The period is made dimensionless using the shear rate $\dot{\gamma}$ and normalised by a factor 2π . Panels: (a) both prolate and oblate, (b) prolate, and (c) oblate particles. The experimental values are displayed as coloured rectangles (cylindrical particles) and circles (spheroidal particles). Each point is the average over all the available experiments for all particle Reynolds numbers ($Re_p \lesssim 1$). The theories of Jeffery (1922) and Burgers (1938), the semi-empirical correlation of Cox (1971), and the empirical expression of Harris & Pittman (1975) are displayed as a solid black line, a dotted cyan line, a dashed blue line and a dash-dotted pink line, respectively. The experiments of Anczurowski & Mason (1968) are displayed as empty grey diamonds (cylinders) and one solid x (spheroid), while the data of Harris & Pittman (1975) correspond to empty brown plus symbols. See Supplementary Materials for the directory of the figure including the data and the Jupyter notebook.

prolate and (c) oblate shapes and focus on the asymptotic limits. The data are obtained by averaging over all the available experiments for all particle Reynolds number ($Re_p \lesssim 1$), meaning that we choose in these plots not to take into account any possible influence of inertia on the period of rotation. Such influence will be addressed later at the end of this section. The data are displayed as empty rectangles for cylindrical particles and circles for spheroidal particles and explore a moderate range of aspect ratios ($0.05 \lesssim r \lesssim 21$). They complement the previous experimental results of Anczurowski & Mason (1968) for disks and fibres (empty grey diamonds) as well as one prolate spheroid (solid grey x), and those of Harris & Pittman (1975) for fibres with higher aspect ratio (empty brown pluses), also reported in the figure.

The present measurements for the period of spheroidal particles span over two decades of r around $r = 1$, extending over the experimental dataset of Anczurowski & Mason (1968). Their agreement with the theory of Jeffery (1922), $T_J \dot{\gamma} = 2\pi(r + 1/r)$, displayed as a solid black curve, is excellent. We remark here that the expression just given can be written as $2\pi/T_J = (\dot{\gamma}/2)\sqrt{1 - \Lambda^2}$ if the Bretherton constant, or shape parameter, $\Lambda = (r^2 - 1)/(r^2 + 1)$ is used. In contrast, the measured period of cylindrical particles systematically lies below the Jeffery curve, meaning that the period of a cylinder is always smaller than that of the corresponding spheroid at the same r . This difference is minimal around $r = 1$ and increases

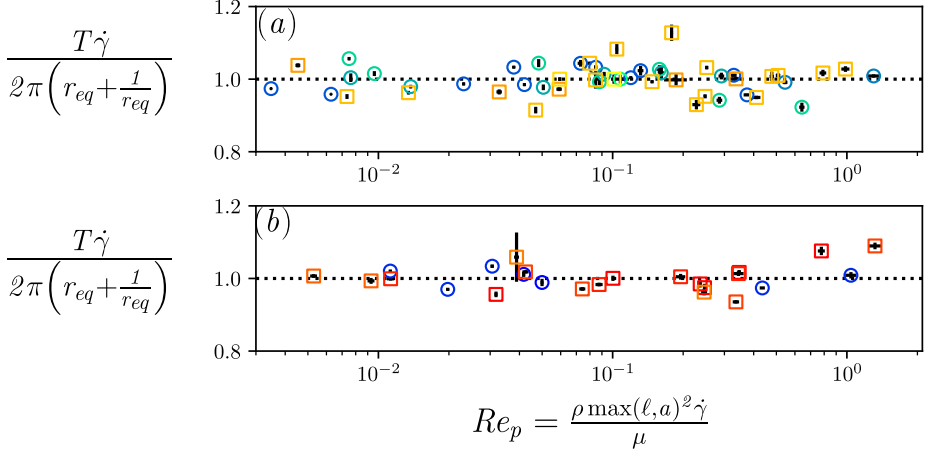


Figure 8: Period of rotation, T , of the axisymmetrical particles against the particle Reynolds number, Re_p for: (a) fibres and prolate spheroids and (b) disks and oblate spheroids. The period is now normalised by the Jeffery period, $2\pi(r_{eq} + 1/r_{eq})/\dot{\gamma}$. The dotted black line corresponds thus to the Jeffery period within this normalisation. The experiments are displayed as coloured rectangles (cylindrical particles) and circles (spheroidal particles) with the same colour code for the aspect ratios as in figure 7. See Supplementary Materials for the directory of the figure including the data and the Jupyter notebook.

with increasing slenderness or flatness but not in the same manner. Interestingly, a shorter period of rotation is measured for the disks than for the fibres, as it is clearly evidenced by comparing the prolate CYL20 ($r = 20.5$) and the oblate CYL005 ($r = 0.05$). These data are in good agreement with those available in the literature (Anczurowski & Mason 1968; Harris & Pittman 1975).

Since the pioneering work of Trevelyan & Mason (1951), it has been suggested that an equivalent aspect ratio, r_{eq} , can be found for cylindrical particles to recover the Jeffery period. In particular, r_{eq} can be computed from $T\dot{\gamma} = 2\pi(r_{eq} + 1/r_{eq})$ using the measured period of rotation for T . Different expressions have been proposed for r_{eq} . In an earlier work for the case of fibres, Burgers (1938) showed that the disturbance caused by a cylinder of axis ratio r will be reproduced by an spheroid of $r_{eq} = 0.74r$, an expression which would eventually diverge at high r as well as underestimate the period of rotation in the near-sphere limit. Our measurements for $10 \lesssim r \lesssim 20$ show good agreement with this proposed equivalence. Later on, by fitting his asymptotic theory to the measurements of Anczurowski & Mason (1968), Cox (1971) provided an expression for slender cylinders as $r_{eq} = 1.24r/\sqrt{\log r}$. Our data are in good agreement with this formula for $r > 5$. Then, Harris & Pittman (1975) proposed an unweighted least square log-log fit over their measurements for slender rods leading to $r_{eq} = 1.14r/r^{0.156}$. They found that Cox's semi-empirical prediction was an overestimate in the asymptotic limit and their power-law function of r showed an excellent agreement with all the considered experimental measurements available at that time. This empirical correlation provides an excellent match with our present data for both prolate and oblate cylinders. It is even accurately predicting the additional measurements with the thinnest disk (CYL005, red rectangle in figure 7).

To conclude this section, we move to the influence of inertia on the period of rotation. Figure 8 shows the period of rotation, T , normalised by the Jeffery period, $2\pi(r_{eq} + 1/r_{eq})/\dot{\gamma}$, against the particle Reynolds number, Re_p . The data are now averaged over experimental runs at the same Re_p for each particle. While r_{eq} is equal to the aspect ratio r for the spheroidal

particles, its value for the cylindrical particles is determined by solving $T\dot{\gamma} = 2\pi(r_{eq} + 1/r_{eq})$ using their measured period of rotation, T , at each Re_p . For both prolate and oblate particles, there is a good collapse of the data around unity, corresponding to the Jeffery period. The data are scattered within $\pm 20\%$ but do not indicate any systematic trend with increasing inertia. We can conclude that inertia does not affect significantly the period of rotation, T , for $Re_p \lesssim 1$, at least within the range of aspect ratios considered in our study. For much longer (very slender) fibres, some alignment might be observed in the presence of small inertia, as the findings of Subramanian & Koch (2005) seem to suggest, the same being possible for very thin disks, as suggested by the results of Rosén *et al.* (2015).

3.3. Drift

Having previously looked at the general behaviours of the Jeffery orbits in figure 6, we now examine in detail the influence of inertia on the time evolution of each component of the orientation vector \mathbf{n} . Figures 9, 10 and 11 display the three components of \mathbf{n} in the flow (n_1), gradient (n_2), and vorticity (n_3) directions against the dimensionless time, $t\dot{\gamma}$. For clarity of presentation, we have chosen to focus the discussion on a subset of three runs for a typical fibre and a disk at a small but finite Re_p and at a larger Re_p as well as for an oblate spheroid at a sole moderate Re_p . We also compare our results with the asymptotic theory of Einarsson *et al.* (2015a) as detailed in § B.1. It is important to stress that, while the theory considers an unbounded system, there is some degree of confinement in the experiments ($\kappa \approx 0.2$) which may affect the stability of the orbits (Rosén *et al.* 2015). Confinement effects are further discussed in § 4.

Let us first examine the influence of inertia on the dynamics of the fibre with aspect ratio $r = 9$ in figure 9. The general tendency is that the fibre drifts out of the vorticity axis towards the tumbling orbit in the plane of shear as evidenced by the systematic decrease of n_3 with successive oscillations. This effect is stronger for intermediate particle orientations, see runs 5 and 8 of panel (a) and runs 13 of panel (b), whereas it may appear somehow irregular for vorticity aligned orbits, see runs 2 of panel (a) and run 14 of panel (b). At small $Re_p = 0.15$, there is a good agreement between the theory and the experiments, see figure 9 (a), suggesting that the range of application of the asymptotic theory of Einarsson *et al.* (2015a) can be extended to finite values of $Re_p \sim O(10^{-1})$ in the case of the fibres. The agreement is inevitably lost at larger values, e.g. $Re_p \sim O(1)$. At such Re_p , a faster drift toward the tumbling orbit is systematically obtained as compared to the experiments, as can be seen from figure 9 (b) in particular for the case of run 13.

The discussion is now repeated for the disk with aspect ratio $r = 0.05$ in figure 10. Most of the runs show a tendency for the disk to drift towards the vorticity axis, i.e. to move towards the spinning orbit where the particle lays flat in the flow-gradient plane. However, a few runs (with carefully-tuned initial conditions) show disks that are just tumbling with their axis in the plane of shear. This confirms that, unlike prolate particles (which are always driven towards the sole limiting tumbling orbit), oblate particles can drift towards two different orbits, the spinning or the tumbling orbits, depending upon their initial orientations. Whereas the theory of Einarsson *et al.* (2015a) successfully predicts the existence of two limiting orbits, it gives a much stronger overestimation of the drift through consecutive orbits for disks than for fibres, even for the smallest values of Re_p studied. This seems to imply that the range of application of the asymptotic theory is more limited in the oblate case than in the prolate case. This is clear in figure 10 (a) for $Re_p = 0.24$, but becomes even more evident in figure 10 (b) for $Re_p = 0.80$. At this larger Re_p , the theory predicts a rapid shift towards aligned positions while the experiments still show rotational behaviours.

Finally, we consider the oblate spheroid ELL06 with $r = 0.6$ at moderate $Re_p = 0.43$ in figure 11. At first glance, no remarkable difference emerges with regards to the slender disk

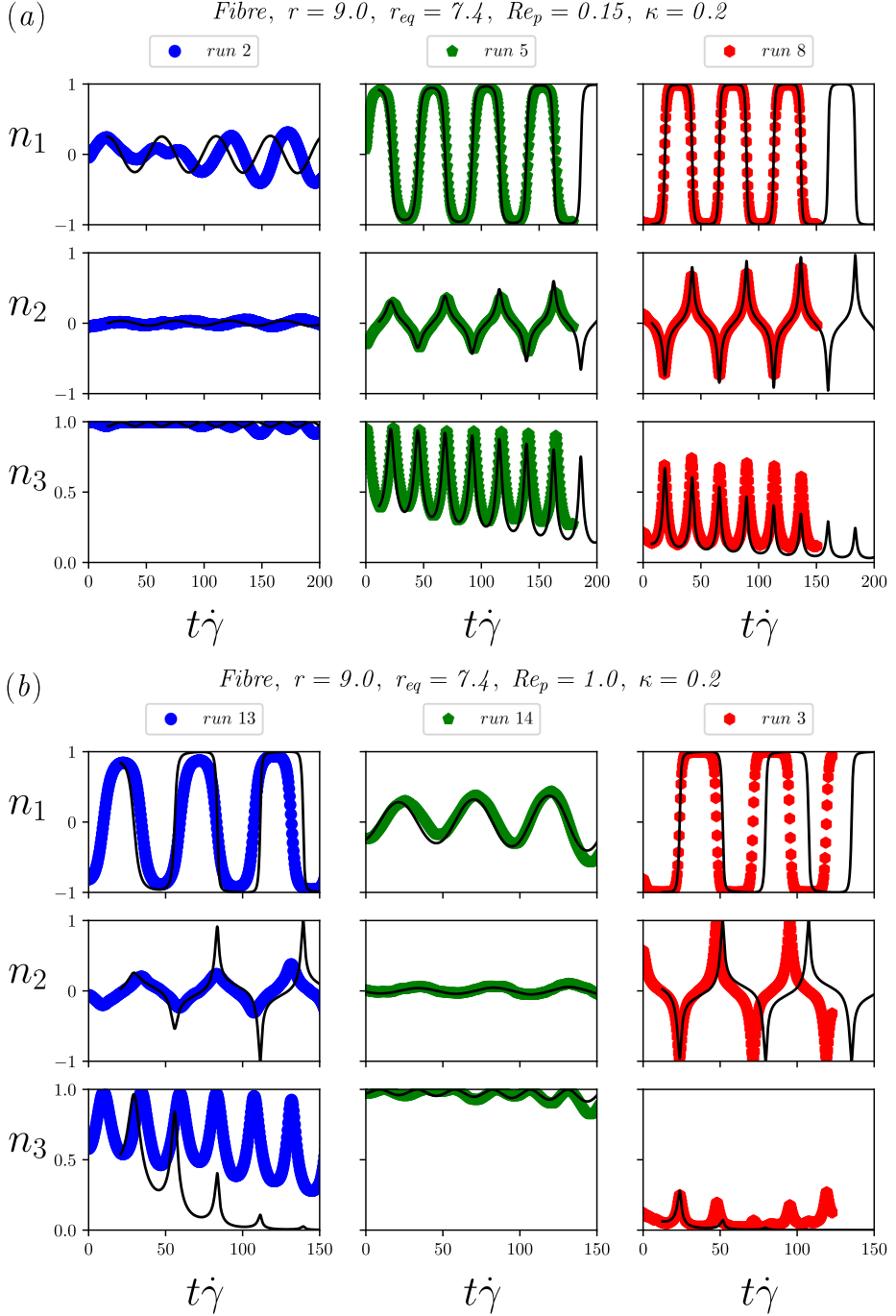


Figure 9: Evolution of the components of the orientation vector \mathbf{n} , displayed as vertically aligned panels for 3 typical runs against the dimensionless time $t\dot{\gamma}$, for the fibre CYL10 with aspect ratio $r = 9$ and confinement ratio $\kappa = 0.19$: (a) $Re_p = 0.15$; (b) $Re_p = 1.0$. Comparison with the theory of Einarsson *et al.* (2015a), presented in § B.1 is also given as black dashed lines. See Supplementary Materials for the directory of the figure including the data and the Jupyter notebook.

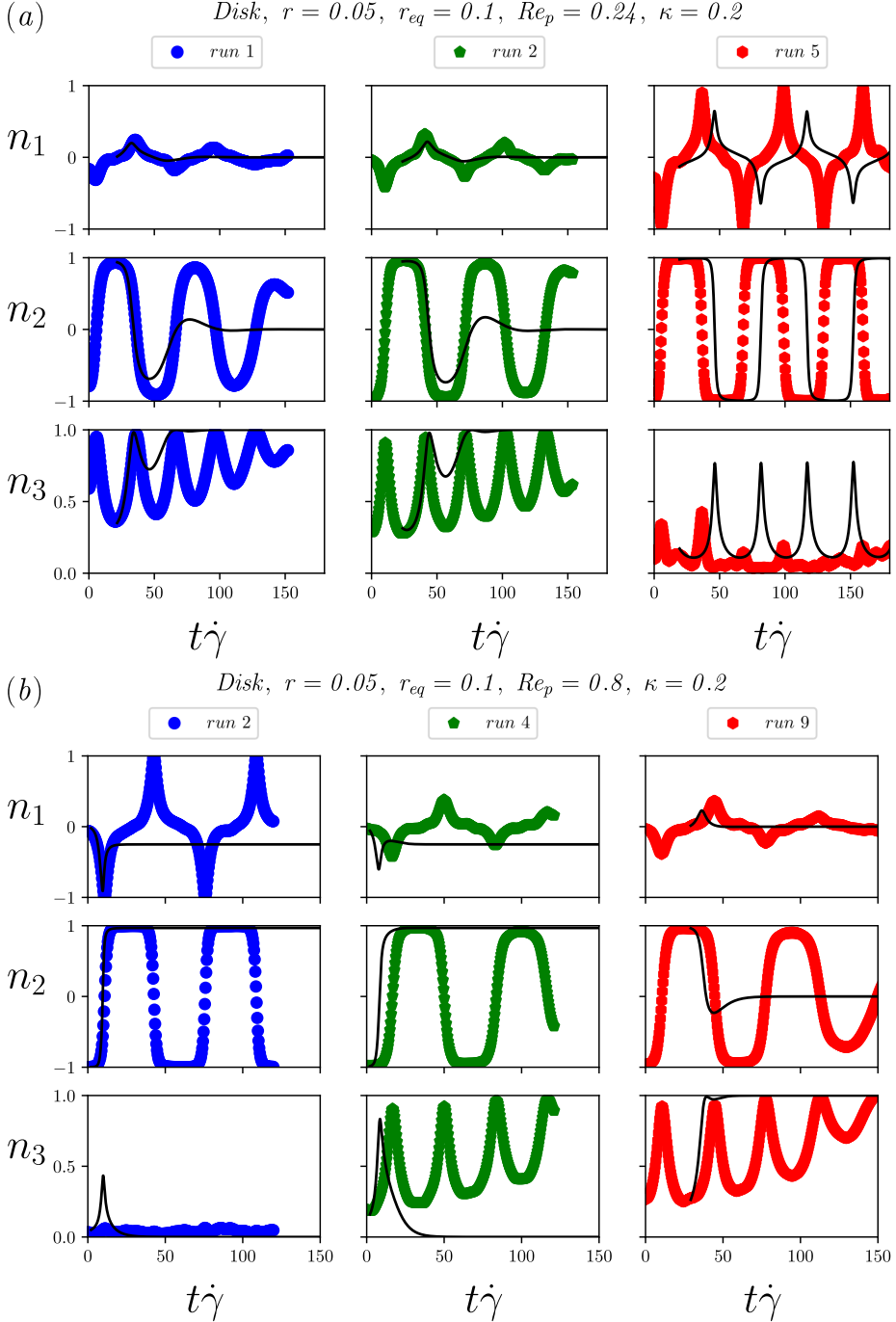


Figure 10: Evolution of the components of the orientation vector \mathbf{n} , displayed as vertically aligned panels for 3 typical runs against the dimensionless time $t\dot{\gamma}$, for the disk CYL005 with aspect ratio $r = 0.05$ and confinement ratio $\kappa = 0.19$: (a) $Re_p = 0.24$; (b) $Re_p = 0.8$. Comparison with the theory of Einarsson *et al.* (2015a), presented in § B.1 is also given as black dashed lines. See Supplementary Materials for the directory of the figure including the data and the Jupyter notebook.

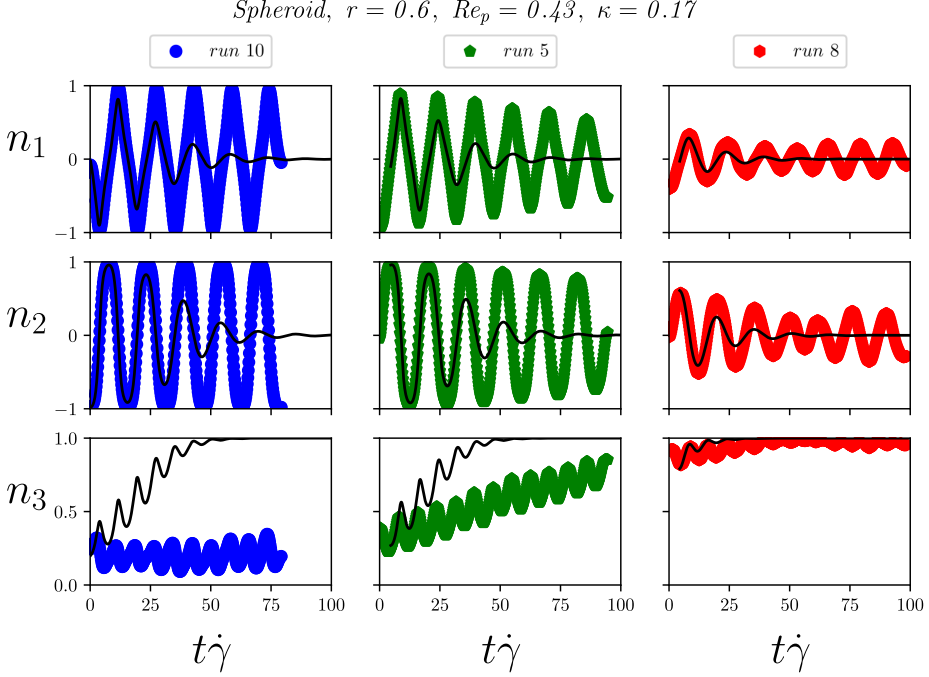


Figure 11: Evolution of the components of the orientation vector \mathbf{n} , displayed as vertically aligned panels for 3 typical runs against the dimensionless time $t\dot{\gamma}$, for the oblate spheroid ELL06 with aspect ratio $r = 0.6$ and confinement ratio $\kappa = 0.17$ at particle Reynolds number $Re_p = 0.43$. Comparison with the theory of Einarsson *et al.* (2015a), presented in § B.1 is also given as black dashed lines. See Supplementary Materials for the directory of the figure including the data and the Jupyter notebook.

CYL005, displayed in figure 10. This spheroid both tumbles in the plane of shear (run 10) or slowly drifts to the spinning orbit (runs 8 and 5). However, in addition to the already discussed discrepancy of the drift, there is a notable difference between the theory of Einarsson *et al.* (2015a) and the experiments regarding the dynamics of this nearly-spherical oblate spheroid. For this type of particle, the asymptotic theory only predicts the drift to an attracting spinning orbit at $Re_p \ll 1$. This is further discussed in connection to confinement effects in §4.

As previously mentioned in §1, the separation between the two limiting orbits for the oblate particles is predicted to depend on their initial orientations but also on their aspect ratio (Einarsson *et al.* 2015b; Dabade *et al.* 2016). To examine this difference in drift more closely and avoid the ambiguity of an arbitrary initial condition, we calculate the change in the orbit constant in a single Jeffery period as done in Dabade *et al.* (2016). As detailed in §2.5, this implies the fitting of our experimental measurements to estimate the local values of the orbit constant C before taking discrete differences ΔC over each period of rotation. The results are shown in figure 12, where the normalised change in the orbit constant in a single period, $Re_p^{-1} \Delta C / (C^2 + 1)$, is plotted against the normalized orbit constant $C / (C + 1)$ for all the experiments. Measurements referring to different values of Re_p are identified by different colours. The values $C / (C + 1) = 0$ and $C / (C + 1) = 1$ correspond to the spinning and tumbling modes, respectively. Following Dabade *et al.* (2016), to keep the drift finite in the near-sphere limit, the normalisation for ΔC also uses a factor depending on the particle eccentricity: $\xi_0 = \sqrt{1/(1 - 1/r^2)}$ for the prolate particles and $\xi_0 = \sqrt{1/(1 - r^2)}$ for the oblate particles.

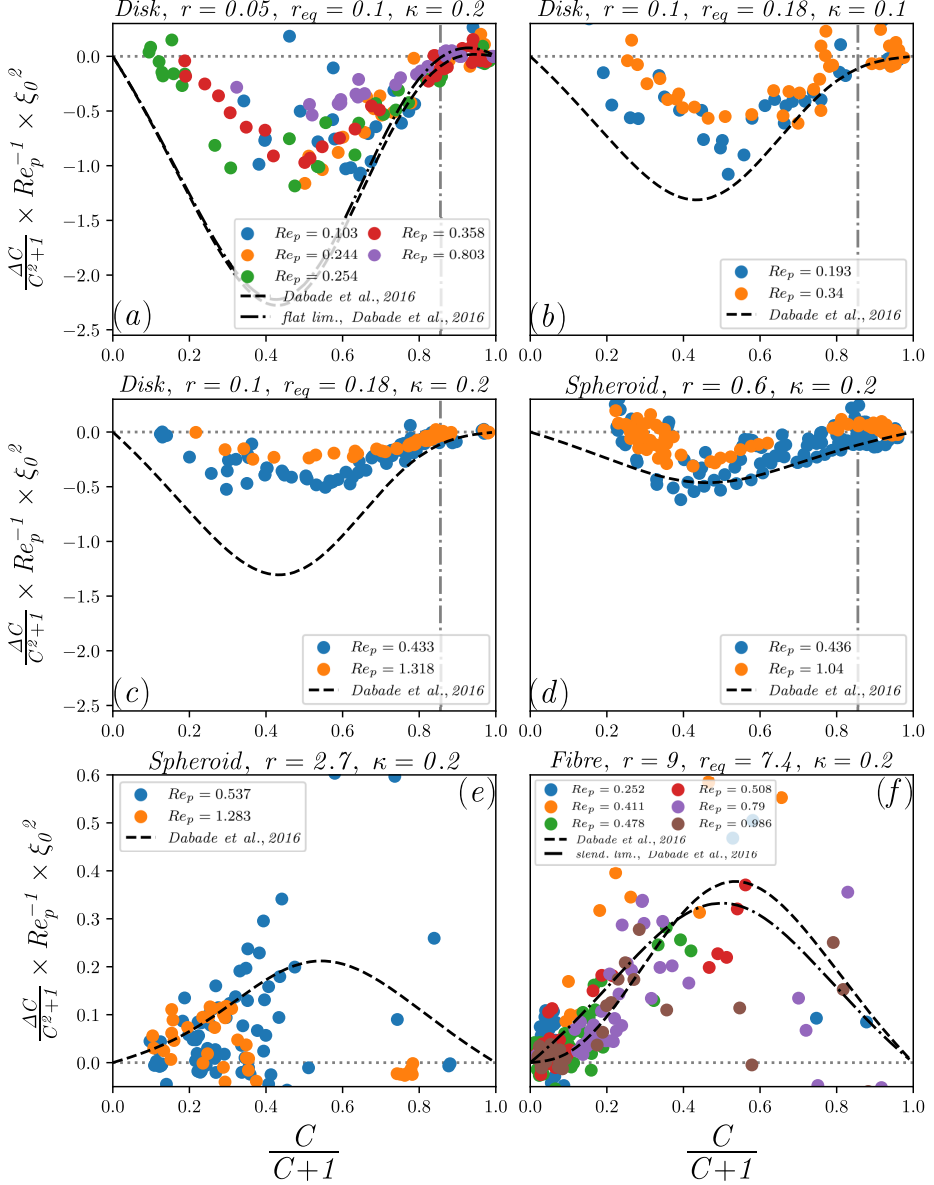


Figure 12: Discrete variation of the orbit constant over one period, ΔC , against the orbit constant C . Results refer to the following particle types (characterised by different colours for the varying Re_p): (a) disk CYL005 ($r = 0.05$ and $\kappa = 0.19$); (b) disk CYL009 ($r = 0.1$ and $\kappa = 0.11$); (c) disk CYL01, ($r = 0.11$ and $\kappa = 0.21$); (d) spheroid ELL06, $r = 0.56$ and $\kappa = 0.17$); (e) spheroid ELL3, ($r = 2.67$ and $\kappa = 0.19$); (f) fibre CYL10, ($r = 9.01$ and $\kappa = 0.19$). The drift is normalised to keep its value finite in the near-sphere limit as in Dabade *et al.* (2016), thus yielding a better comparison with their theory (black dashed line and black solid line in the slender limit). The predicted critical orbit constant $C^* = \sqrt{35}$, i.e. $C^*/(C^* + 1) \simeq 0.86$, separating the basins of attracting in the slender disk limit is also displayed as a dash-dotted grey line (Dabade *et al.* 2016). Data are collected over all the available experiments at a given Re_p (up to 10 runs), measuring the orbit constant and its variation as described in § 2.5. See Supplementary Materials for the directory of the figure including the data and the Jupyter notebook.

Figure 12 displays results for the following cases: the thinnest disk with $r = 0.05$ in panel (a), two disks having similar r but two different confinement ratios in panels (b) ($r = 0.1, \kappa = 0.1$) and (c) ($r = 0.11, \kappa = 0.2$), a thicker oblate spheroid with $r = 0.56$ in panel (d). Also included are the results for two prolate particles: a prolate spheroid with $r = 2.7$ in panel (e) and a slender fibre with $r = 9$ in panel (f). These data are compared to the theoretical prediction of Dabade *et al.* (2016) considering both particle and fluid inertia ($St = Re_p$ in the present neutrally-buoyant case) as detailed in § B.2.

Despite the rather large scatter of the data, there are some clear trends and qualitative agreements with theoretical predictions. Prolate particles experience positive increments of the orbit constant, which drive them towards tumbling motion ($C = \infty$, namely $C/(C+1) = 1$), while oblate particles experience negative variations as they are mostly attracted to the vorticity-aligned orbit ($C = 0$, namely $C/(C+1) = 0$). Moreover, as revealed from the scales of the ordinate axes, the drift intensity ΔC increases with the aspect ratio r , as more slender objects experience more unstable Jeffery orbits.

The oblate particles not only drift towards the spinning orbit but also to the tumbling orbit as evidenced by the clustering of points around zero and slightly above for orbit constants $C \gtrsim \sqrt{35}$, namely $C/(C+1) \gtrsim 0.86$, as computed by Dabade *et al.* (2016), see panels (a) to (c). This is in stark contrast with the strong incline taken by the fibre of aspect ratio $r = 9$ in panel (f) when leaving the spinning orbit ($C/(C+1) = 0$) which is unstable for this prolate particle.

An interesting behaviour is observed in panel (d) for the oblate spheroid with $r = 0.6$, a value well above the predicted critical aspect ratio of approximately 0.14 for which only drift toward the spinning motion is anticipated. As evidenced in figure 11, this particle is still experiencing tumbling and spinning orbits, in contradiction with theoretical predictions. The critical orbit constant seems also to have moved as positive increments of orbit constant are observed at $C \lesssim \sqrt{35}$, i.e. $C/(C+1) \lesssim 0.86$, in particular for the higher Re_p . Similar behaviour is observed for the disk with $r_{eq} = 0.18$ in panels (b) and (c), which correspond to different confinements. This may suggest a wider region of attraction for the tumbling mode.

The influence of confinement is clearly visible between panels (b) and (c), where are shown two disks at a comparable $r \approx 0.1$ but differing confinement ratios, $\kappa = 0.11$ and $\kappa = 0.21$. The smaller disk is in better agreement with the theory than the large disk having a twofold increase of confinement ratio, where the drift is less intense than that predicted by Dabade *et al.* (2016) for an unconfined viscous shear flow.

Finally, we address the scaling of the drift intensity with the particle Reynolds number. Clearly, experiments at higher particle Reynolds number ($Re_p \approx 1$) do not collapse with those at smaller Re_p . Despite the large scatters, this is particularly evidenced in panels (a),(c),(d) for oblate objects, where the intensity of the drift is weaker for the larger Re_p . This suggests a saturation effect above a certain inertial threshold.

4. Concluding remarks

We have examined the rotation of axisymmetrical particles suspended in a simple shear flow when inertia is progressively increased up to particle Reynolds number $Re_p \approx 1$. A custom-built shearing cell and a multi-view reconstruction method have been used to obtain direct measurements of the orientation and period of rotation of ideal bodies such as spheroids but also bodies of practical interest such as cylinders with different aspect ratios. This system is rather flexible and is amenable to study the alignment of small bodies with different shapes in simple shearing flows.

The first important result is that the axisymmetric particles still rotate with the Jeffery

period in this small-inertia regime. Our results also complement the data available in the literature (Anczurowski & Mason 1968; Harris & Pittman 1975) and provide a connection with those of Zettner & Yoda (2001) at higher Re_p , showing that the period of rotation of a cylinder is smaller than that of an spheroid with the same aspect ratio. An equivalent spheroidal aspect ratio can be inferred to recover the Jeffery period in the case of cylinders. Our results show that the empirical expression of Harris & Pittman (1975) still remains the best prediction for this equivalent aspect ratio, which we were able to validate over one further decade of slender oblate particles compared to available literature results.

The second major output is that we observe an irreversible drift across Jeffery orbits towards attracting limiting cycles. This drift is due to weak inertial effects, and its occurrence confirms, at least qualitatively, the asymptotic theories of Einarsson *et al.* (2015b) and Dabade *et al.* (2016). It is important to stress before proceeding to any comparison below that these theories are meant to be valid for $Re_p \ll 1$ as well as at infinite distance from walls. Clearly, some deviations between their predictions and experimental results begin to appear as one moves away from their range of validity as discussed below.

Our measurements indicate that prolate particles are uniquely driven towards a tumbling motion in the flow-gradient plane regardless of their initial orientation and aspect ratio. For small but finite Re_p , i.e. typically up to $O(10^{-1})$ in our experiments, there is a good quantitative agreement with the theories. For larger Re_p , i.e. of $O(1)$ in our experiments, a saturation of the phenomenon is observed and the asymptotic theories predict a faster drift toward the tumbling orbit. This is expected since these theories are strictly valid only for $Re_p \ll 1$ and cannot be expected to describe the dynamics at Re_p of order unity or larger, as also discussed in Rosén *et al.* (2015).

In stark contrast to prolate particles, which only possess a single attracting orbit, oblate particles are observed to drift towards two different orbits, the spinning orbit or the tumbling orbit, depending upon their initial orientation. Whereas the theories of Einarsson *et al.* (2015b) and Dabade *et al.* (2016) do predict the existence of two limiting orbits, their overestimation of the drift through consecutive orbits is more severe and even seen for small Re_p of $O(10^{-1})$ as also discussed in Rosén *et al.* (2015) when the theory is compared to DNS results. This may suggest that the predictive capabilities of the theories in the small-inertia regime are more limited for oblate particles and that their range of application at finite Re_p is narrower than for prolate particles. We remark here that part of the observed overestimation may be ascribed to unavoidable confinement effects (Rosén *et al.* 2015), which tend to lower the drift intensity and thus introduce a small bias in the experimental measurements. Again, it seems that these effects do affect more the oblate particles.

There is a notable discrepancy between the experiments and the predictions of Einarsson *et al.* (2015b) and Dabade *et al.* (2016) regarding the stability of the tumbling orbit for oblate particles. A bifurcation toward a single stable spinning orbit above a critical aspect ratio of approximately 0.14 is not observed, suggesting a wider basin of attraction for the tumbling mode in the experiments for small Re_p of $O(10^{-1})$ up to $O(1)$. The time-resolved simulations of Rosén *et al.* (2015) having a confinement of $\kappa = 0.2$ have shown a bifurcation between stable and unstable tumbling for a critical aspect ratio of approximately 0.13 at $Re_p = 1$, in fair agreement with the prediction 0.14 of the asymptotic theories. Rosén *et al.* (2015) even tracked the bifurcation for larger Re_p , showing that it can survive up to $Re_p = 5$, see the bifurcation diagram of their figure 4. Our experimental results for similar confinement ($\kappa = 0.2$) and even those with smaller confinement ($\kappa = 0.1$) still exhibit stable tumbling modes. While this finding is intriguing, it seems reasonable to assume that it cannot be attributed to confinement.

Overall, our results indicate that inertia plays a significant role in breaking the indeterminacy of the Jeffery orbits for the prolate particles, while we still observe the existence of two

limiting orbits for the oblate particles. This finding has deep consequences for the steady-state rheology of suspensions of axisymmetrical particles in a viscous dilute regime, i.e. when particle-particle interactions are negligible. Indeed, prolate particles will eventually drift toward the tumbling orbit, aligning asymptotically with the mean flow direction. Conversely, the effective viscosity of a suspension of oblate particles will always depend on their initial orientation and regardless of their aspect ratio, i.e. not only in the lower near-sphere limit ($0.14 < r < 1$) as predicted by Dabade *et al.* (2016). Of course, hydrodynamic and direct particle-particle interactions come into play and change the picture as soon as semi-dilute and concentrated suspensions are considered (Butler & Snook 2018).

A final comment is in order about the importance of including the effect of both the fluid and particle inertia in the numerical calculation of the rotational dynamics of axisymmetric particles suspended in complex flows, e.g. turbulent flows. In a turbulent flow, the modified rotation rate (see equation B 1) might affect the distribution of particle orientations (Sheikh *et al.* 2020). In homogeneous isotropic turbulence, axisymmetric prolate (*resp.* oblate) particles were seen to align with (*resp.* perpendicular to) the local vorticity vector, following the local flow stretching in a mostly spinning (*resp.* tumbling) rotational state (Ni *et al.* 2015; Byron *et al.* 2015). Accounting for the inertial torques would strengthen the influence of the local stretching, even if one might argue under which conditions the inertial contribution becomes relevant given the intermittent nature of the flow. One may indeed need to compare the drift time (of typical order of a few periods of rotation) with the typical time of the flow velocity fluctuations. The picture is even more complex in bounded turbulence, where the strong near-wall shear causes axisymmetric particles to follow the local flow stretching but aligns the vorticity vector in the spanwise direction (Zhao & Andersson 2016). In this case, inertial torques could especially modify the orientation statistics of oblate particles, which tend to align normal to the wall, with possible consequences for drag reduction (Wang *et al.* 2021).

Supplementary data. Supplementary material and movies are available at <https://doi.org/10.1017/jfm.2023...>

Acknowledgements. We thank N. K. Marath and G. Subramanian for providing detailed information on their calculation for the drift of oblate spheroids.

Funding. D.D.G. acknowledges the Università Italo-Francese, Bando Vinci 2021, cap. 2, progetto C2-257 ‘Fibre flessibili in flusso turbolento ad elevato numero di Reynolds’ for the generous funding.

Declaration of interests. The authors report no conflict of interest.

Data availability statement. The data that support the findings of this study are openly available in [repository name] at [http://doi.org/\[doi\]](http://doi.org/[doi]), reference number [reference number].

Author ORCIDs.

Davide Di Giusto <https://orcid.org/0000-0003-4413-2454>;
 Laurence Bergougnoux <http://orcid.org/0000-0002-2988-4394>;
 Cristian Marchioli <https://orcid.org/0000-0003-0208-460X>;
 Élisabeth Guazzelli <http://orcid.org/0000-0003-3019-462X>.

Appendix A. Three-dimensional particle orientation estimation

A.1. Three-dimensional Axis-Aligned Bounding Box (AABBB) calculation for cylinders and spheroids

In this section we briefly describe the geometrical relations that provide the AABBB for cylindrical and spheroidal particles, having imposed their orientation vector \mathbf{n} . The relation is straightforward for cylinders, whose projection corresponds to the sum of a line and two

620 capping circles (Quilez 2016). The eccentricity e of these two circles is defined as:

$$621 \quad e = a \cdot \sqrt{1 - \mathbf{n} \cdot \mathbf{n}} . \quad (\text{A } 1)$$

622 Given the centre points of the capping circles, \mathbf{p}_a and \mathbf{p}_b , \mathbf{B} is obtained by maximising the
623 only possible orientation extension:

$$624 \quad \mathbf{B} = \max ((\mathbf{p}_a + e), (\mathbf{p}_b + e)) - \min ((\mathbf{p}_a - e), (\mathbf{p}_b - e)) . \quad (\text{A } 2)$$

625 Performing the same calculation for spheroidal particles is slightly more complex, in view
626 of the lack of sharp edges. A generic spheroid that can only rotate but not translate may be
627 represented as a diagonal matrix. If the spheroid is initially aligned with the z axis such that
628 its orientation vector is $\mathbf{n} = (0, 0, 1)$, then the matrix reads as follows:

$$629 \quad \overline{\mathbf{O}} = \begin{bmatrix} a^{-2} & 0 & 0 \\ 0 & a^{-2} & 0 \\ 0 & 0 & (a \cdot r)^{-2} \end{bmatrix} . \quad (\text{A } 3)$$

630 Neglecting the spin, any generic orientation attained by the spheroid can be determined by a
631 combination of the two polar angles ϕ and θ :

$$632 \quad \mathbf{n} = (\sin \phi \sin \theta, \cos \phi \sin \theta, \cos \theta) . \quad (\text{A } 4)$$

633 It is straightforward to build a rotation matrix that correlates the initial orientation of the
634 spheroid to the new one through equation (A 4). Therefore, the quadratic form of the spheroid
635 will also be rotated according to the new orientation as follows:

$$636 \quad \overline{\mathbf{Q}} = \overline{\mathbf{R}} \cdot \overline{\mathbf{O}} \cdot \overline{\mathbf{R}}^T . \quad (\text{A } 5)$$

637 Given the matrix $\overline{\mathbf{Q}}$, in Appendix A.3 we demonstrate that taking the square root of the
638 diagonal components of its inverse yields the halved sides of the AAB: B:

$$639 \quad \mathbf{B}_i = 2 \cdot \sqrt{\overline{\mathbf{Q}}_{i,i}^{-1}} . \quad (\text{A } 6)$$

640 The procedure just described is repeated over $360 \times 360 = 129600$ possible combinations
641 of values of ϕ and θ , in order to discretise any possible orientation in the first quadrant
642 of the three-dimensional Cartesian system. This results in a resolution of 0.25° for each
643 angle. Calculations are scripted in Python to generate extended data sets of AABs and
644 their corresponding orientation vectors. The corresponding scripts are provided in the
645 Supplementary Materials.

646 A.2. Orientation reconstruction by multi-variable regression

647 The relation between the Axis-Aligned Bounding Box \mathbf{B} and the particle orientation vector
648 \mathbf{n} is non-linear and known in a closed form only for the inverse transformation. Therefore, to
649 solve the direct transformation, we choose a data-driven approach.

650 A Deep Learning model is trained using synthetic data generated geometrically as
651 described in the previous section. The model is implemented as a neural network in
652 TensorFlow (Abadi 2015), and performs a multi-variable regression, where the input is
653 an experimentally measured AAB and the output is the corresponding orientation vector \mathbf{n} .
654 Hidden dense layers are made of 256 fully connected weights, introducing non-linearity
655 through the *relu* activation function. Typically, one hidden layer would be sufficient for the
656 regression of the most slender shapes, however, three layers seem preferable to be able to
657 deal also with the nearly spherical objects, e.g. the spheroid ELL06. Normalization of the
658 Euclidean norm of the output orientation vector \mathbf{n} is finally ensured by a dedicated Lambda

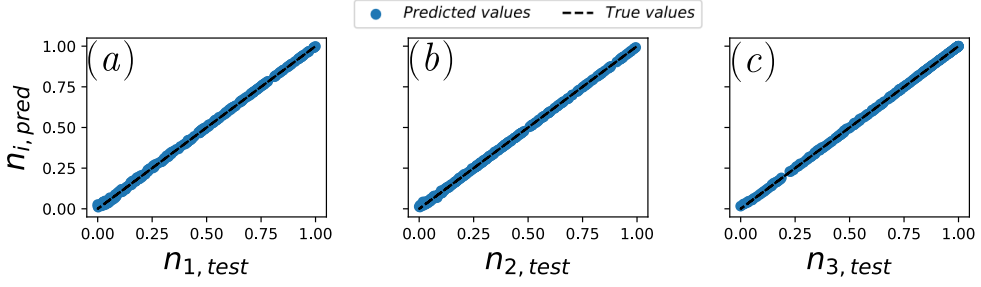


Figure 13: Predicted values against true values of the orientation vector \mathbf{n} obtained applying the Deep Learning model described in Appendix A.2 to a fibre with aspect ratio $r = 9.01$ (CYL10): (a) n_1 along x , (b) n_2 along y , (c) n_3 along z .

layer. The model is compiled and normally trained over at least 20 epochs by minimising a Custom Loss Function (CLF), which calculates the Euclidean norm of the difference between the true and predicted values of the orientation vector \mathbf{n} :

$$CLF = \sqrt{\sum_{i=1}^3 (\mathbf{n}_{true,i} - \mathbf{n}_{pred,i})^2}. \quad (\text{A } 7)$$

In addition, the custom loss function strongly penalises any prediction yielding non-physical, lower-than-zero values for the orientation vector components. The chosen optimisation method is *Adam*, which is a randomized batched Gradient Descent method. A random 20% splitting of the data set between training and testing samples is selected for the training. As displayed in figure 13, the regression for a fibre of aspect ratio $r = 9.01$ (CYL10) is highly reliable and yields precise estimations of the three components of the orientation vector \mathbf{n} . It is important to stress that the lack of availability of previously measured similar experiments prevents us from further testing the model. The Python script used to estimate the particle orientation vector \mathbf{n} from its AABBs is provided in the Supplementary Materials.

A.3. Relation between the Axes-Aligned Bounding Box of an spheroid and the principal diagonal terms of its matrix of coefficients.

Given a generic n -dimensional hyper-spheroid \mathcal{E} :

$$\mathcal{E} = \{x \in \mathbb{R}^n | (x - c)^T Q^{-1} (x - c) \leq 1\}, \quad (\text{A } 8)$$

where $c \in \mathbb{R}^n$ is the vector defining the centre of the spheroid and Q is a positive definite matrix of coefficients, and writing $g(x) = (x - c)^T Q^{-1} (x - c)$, the vector field orthogonal to the shell of the spheroid is:

$$\nabla g(x) = 2Q^{-1} (x - c). \quad (\text{A } 9)$$

Considering the i^{th} axis and the corresponding projection matrix $P_i = e_i e_i^T$, the orthogonal vector field $\nabla g(x)$ and its projection $P_i \nabla g(x)$ will satisfy the condition:

$$\nabla g(x) = P_i \nabla g(x), \quad (\text{A } 10)$$

at the two points where the spheroid \mathcal{E} touches the (smallest) bounding box, namely the smallest AABB. The above condition is equivalent to:

$$(I_n - P_i) \underbrace{Q^{-1} (x - c)}_{\equiv y} = 0_n, \quad (\text{A } 11)$$

where the entry y_i will be the only non-zero value, i.e. $y = te_i$, or $x = c + tQe_i$. Intersecting this line with the boundaries of the spheroid, t can be obtained as follows:

$$t^2 = (e_i^T Q e_i)^{-1} = q_{ii}^{-1}, \quad (\text{A } 12)$$

where q_{ii} is the i^{th} entry of the inverse of the matrix Q . Therefore, the shell of the i^{th} projection of the spheroid will touch the smallest AABB at the following two points:

$$x_i = c_i \pm \frac{1}{\sqrt{q_{ii}}} e_i^T Q e_i = c_i \pm \frac{q_{ii}}{\sqrt{q_{ii}}} = c_i \pm \sqrt{q_{ii}}. \quad (\text{A } 13)$$

Appendix B. Comparison with small-inertia theories

B.1. Model of Einarsson et al. (2015a)

Einarsson *et al.* (2015a) characterised the influence of inertia on Jeffery orbits as additional terms to equation (1.1), which then reads as:

$$\begin{aligned} \dot{\mathbf{n}} = & \mathbf{\Omega} \cdot \mathbf{n} + \frac{r^2 - 1}{r^2 + 1} [\mathbf{E} \cdot \mathbf{n} - \mathbf{n} (\mathbf{n} \cdot \mathbf{E} \cdot \mathbf{n})] + \beta_1 (\mathbf{n} \cdot \mathbf{E} \cdot \mathbf{n}) \mathbb{P}(\mathbf{E} \cdot \mathbf{n}) + \\ & + \beta_2 (\mathbf{n} \cdot \mathbf{E} \cdot \mathbf{n}) \mathbf{\Omega} \cdot \mathbf{n} + \beta_3 \mathbb{P}(\mathbf{\Omega} \cdot \mathbf{E} \cdot \mathbf{n}) + \beta_4 \mathbb{P}(\mathbf{E} \cdot \mathbf{E} \cdot \mathbf{n}), \end{aligned} \quad (\text{B } 1)$$

where $\mathbb{P}(\mathbf{x}) = \mathbf{x} - (\mathbf{n} \cdot \mathbf{x}) \mathbf{n}$ is an operator that projects components in the \mathbf{n} -direction. The first two terms on right-end side of equation (B 1) correspond to the original Jeffery equation while the last four terms, each containing a scalar coefficient β_i , are the inertia-related terms. The coefficients β_i are functions of the particle aspect ratio, provided graphically in figure 2 of Einarsson *et al.* (2015b) for $Re_p = St$ and reported here in figure 14 for the CYL10 case, using the equivalent aspect ratio for cylinders. Equation (B 1) is integrated in time using the odeint function of the Scipy Python library. The initial conditions are provided by the first flow-aligned orientation measured in the CYL10 experimental run. The Python script used to solve for equation (B 1) is provided in the Supplementary Materials.

B.2. Model of Dabade et al. (2016)

Dabade *et al.* (2016) characterize the inertia-driven drift from the Jeffery orbits through consecutive rotations by means of discrete variations of the orbit constant ΔC in a single Jeffery period. For particle inertia, this is given in their equation (5.19) in terms of the eccentricity: $\xi_0 = \sqrt{1/(1 - 1/r^2)}$ for the prolate and $\xi_0 = \sqrt{1/(1 - r^2)}$ for the oblate particles. The eccentricity parameter ξ_0 is calculated using the physical particle aspect ratio, r , for the spheroids and the equivalent particle aspect ratio, r_{eq} , for the cylinders, obtained by averaging over all the available experiments. Then, the integrals I_i, J_i are provided in Appendix C, while the prolate F_i^p, G_i^p coefficients come from their equations (5.7-5.12). Following Dabade *et al.* (2016) to obtain the oblate coefficients, one needs first to multiply the prolate coefficients by the squared length-scale to obtain their dimensional form. Then the transformation prolate-to-oblate must be applied ($\xi_0 < - > i (\xi_0^2 - 1)^{0.5}$), before returning to dimensionless variables by dividing by the squared length-scale, as described below equation (5.12) of Dabade *et al.* (2016). The fluid-inertia drift is still obtained from equation (5.19), where St is replaced by Re_p and the F_i^f, G_i^f coefficients are given in equations (6.1-6.8). The Python script used to calculate the discrete orbit variation ΔC as in Dabade *et al.* (2016) is provided in the Supplementary Materials.

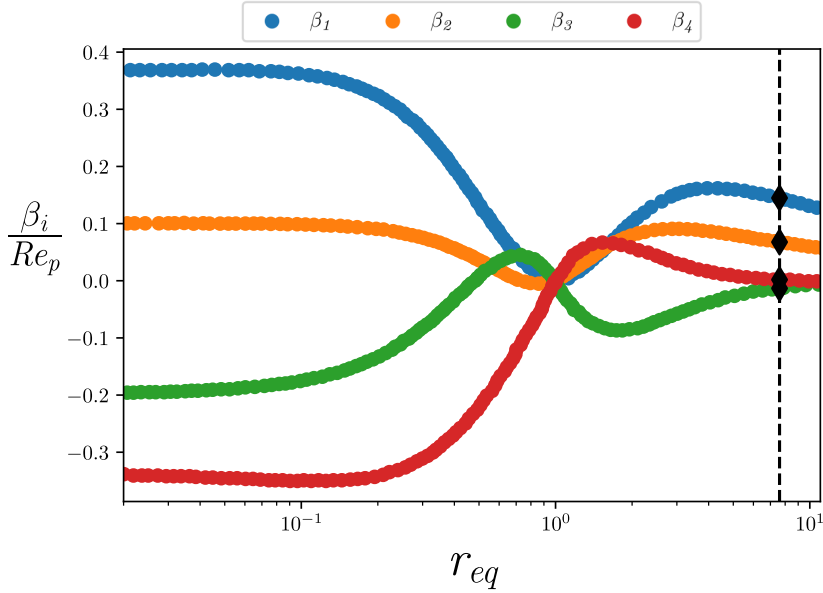


Figure 14: β_i coefficients of equation B 1 as given in Figure 2 of Einarsson *et al.* (2015b).
As an example, for the fibre CYL10, the coefficients β_i are chosen at the intersection between the dotted vertical line at $r_{eq} = 7.4$ with the respective curves.

- 724 ABADI, M. 2015 TensorFlow: Large-scale machine learning on heterogeneous systems. Software available
725 from tensorflow.org.
- 726 ANCZUROWSKI, E. & MASON, S. G. 1968 Particle motions in sheared suspensions. xxiv. rotation of rigid
727 spheroids and cylinders. *Trans. Soc. Rhe.* **12** (2), 209–215.
- 728 BAO, G., HUTCHINSON, J. W. & McMEEKING, R. M. 1991 Particle reinforcement of ductile matrices against
729 plastic flow and creep. *Acta Met. Mat.* **39** (8), 1871–1882.
- 730 BINDER, R. C. 1939 The motion of cylindrical particles in viscous flow. *J. of App. Phys.* **10** (10), 711–713.
- 731 BRADSKI, G. 2000 The OpenCV Library. *Dr. Dobbs's Journal of Software Tools*.
- 732 BRETHERTON, F P 1962 The motion of rigid particles in a shear flow at low reynolds number. *J. Fluid Mech.*
733 **14** (2), 284–304.
- 734 BURGERS, J. M. 1938 Second report on viscosity and plasticity **16**, 113–84.
- 735 BUTLER, J. E. & SNOOK, B. 2018 Microstructural dynamics and rheology of suspensions of rigid fibers. *Ann.*
736 *Rev. Fluid Mech.* **50**, 299–318.
- 737 BYRON, M., EINARSSON, J., GUSTAVSSON, K., VOTH, G. A., MEHLIG, B. & VARIANO, E. 2015 Shape-
738 dependence of particle rotation in isotropic turbulence. *Phys. Fluids* **27** (3), 035101.
- 739 CANNY, J. 1986 A computational approach to edge detection. *IEEE Trans. Patt. an. and mach. intel.* **6**,
740 679–698.
- 741 COX, R. G. 1971 The motion of long slender bodies in a viscous fluid. part 2. shear flow. *J. Fluid Mech.*
742 **45** (4), 625–657.
- 743 DABADE, V., MARATH, N. K. & SUBRAMANIAN, G. 2016 The effect of inertia on the orientation dynamics of
744 anisotropic particles in simple shear flow. *J. Fluid Mech.* **791**, 631–703.
- 745 DU ROURE, O., LINDNER, A., NAZOCKDAST, E. N. & SHELLEY, M. J. 2019 Dynamics of flexible fibers in
746 viscous flows and fluids. *Annu. Rev. Fluid Mech.* **51**, 539–572.
- 747 EBERLY, D. 1999 Least squares fitting of data by linear or quadratic structures. *Geom. Tools, July*.
- 748 EINARSSON, J., CANDELIER, F., LUNDELL, F., ANGILELLA, J. R. & MEHLIG, B. 2015a Effect of weak fluid
749 inertia upon jeffery orbits. *Phys. Rev. E* **91** (4), 041002.
- 750 EINARSSON, J., CANDELIER, F., LUNDELL, F., ANGILELLA, J. R. & MEHLIG, B. 2015b Rotation of a spheroid
751 in a simple shear at small reynolds number. *Phys. Fluids* **27** (6), 063301.
- 752 EINARSSON, J., MIHIRETIE, B. M., LAAS, A., ANKARDAL, S., ANGILELLA, J. R., HANSTORP, D. & MEHLIG, B.
753 2016 Tumbling of asymmetric microrods in a microchannel flow. *Phys. Fluids* **28** (1), 013302.

- EINSTEIN, A. 1906 Eine neue bestimmung der moleküldimensionen. *Ann. Physik* **19**, 289–306.
- EINSTEIN, A. 1911 Berichtigung zu meiner arbeit: Eine neue bestimmung der moleküldimensionen. *Ann. Physik* **34**, 591–592.
- FORGACS, O. L. & MASON, S. G. 1959 Particle motions in sheared suspensions: X. orbits of flexible threadlike particles. *J. Colloid Sci.* **14** (5), 473–491.
- FRIES, J., EINARSSON, J. & MEHLIG, B. 2017 Angular dynamics of small crystals in viscous flow. *Phys. Rev. Fluids* **2**, 014302.
- GLENDINNING, P. 1994 *Stability, instability and chaos: an introduction to the theory of nonlinear differential equations*, pp. 145,158. Cambridge university press.
- GOLDSMITH, H. L. 1996 The microrheology of dispersions: application to blood cells. *J. Jap. Soc. Biorhe.* **10** (4), 15–36.
- GOLDSMITH, H. L. & MASON, S. G. 1962a The flow of suspensions through tubes. i. single spheres, rods, and discs. *J. Colloid Sci.* **17** (5), 448–476.
- GOLDSMITH, H. L. & MASON, S. G. 1962b Particle motions in sheared suspensions xiii. the spin and rotation of disks. *J. Fluid Mech.* **12** (1), 88–96.
- GUASTO, J. S., RUSCONI, R. & STOCKER, R. 2012 Fluid mechanics of planktonic microorganisms. *Annu. Rev. Fluid Mech.* **44**, 373–400.
- GUSTAVSSON, K., JUCHA, J., NASO, A., LÉVÊQUE, E., PUMIR, A. & MEHLIG, B. 2017 Statistical model for the orientation of nonspherical particles settling in turbulence. *Phys. Rev. Lett.* **119**, 25 (25), 254501.
- HARRIS, J. B. & PITTMAN, J. F. T. 1975 Equivalent ellipsoidal axis ratios of slender rod-like particles. *J. Colloid Interface Sci.* **50** (2), 280–282.
- HOYT, J. W. 1972 Turbulent flow of drag-reducing suspensions. *Tech. Rep.*. NAVAL UNDERSEA CENTER, SAN DIEGO, CA.
- HUANG, H., YANG, X., KRAFCZYK, M. & LU, X.Y. 2012 Rotation of spheroidal particles in couette flows. *J. Fluid Mech.* **692**, 369–394.
- JEFFERY, G. B. 1922 The rotation of two circular cylinders in a viscous fluid. *Proc. R. Soc. Lond. A* **101** (709), 169–174.
- KARNIS, A., GOLDSMITH, H. L. & MASON, S. G. 1963 Axial migration of particles in poiseuille flow. *Nature* **200** (4902), 159–160.
- KARNIS, A., GOLDSMITH, H. L. & MASON, S. G. 1966 The flow of suspensions through tubes, v. inertial effects. *Can. J. Chem. Eng.* **44** (4), 181–193.
- LEAL, L. G. & HINCH, E. J. 1971 The effect of weak brownian rotations on particles in shear flow. *J. Fluid Mech.* **46** (4), 685–703.
- LUNDELL, F., SÖDERBERG, L. D. & ALFREDSSON, P. H. 2011 Fluid mechanics of papermaking. *Annu. Rev. Fluid Mech.* **43**, 195–217.
- MAO, W. & ALEXEEV, A. 2014 Motion of spheroid particles in shear flow with inertia. *J. Fluid Mech.* **749**, 145–166.
- MARATH, N. K. & SUBRAMANIAN, G. 2017 The effect of inertia on the time period of rotation of an anisotropic particle in simple shear flow. *J. Fluid Mech.* **830**, 165–210.
- MARATH, N. K. & SUBRAMANIAN, G. 2018 The inertial orientation dynamics of anisotropic particles in planar linear flows. *J. Fluid Mech.* **844**, 357–402.
- MARCHIOLI, C., BHATIA, H., SARDINA, G., BRANDT, L. & SOLDATI, A. 2019 Role of large-scale advection and small-scale turbulence on vertical migration of gyrotactic swimmers. *Phys. Rev. Fluids* **4**, 124304.
- METZGER, B. & BUTLER, J. E. 2012 Clouds of particles in a periodic shear flow. *Phys. Fluids* **24** (2), 021703.
- MOSES, K. B., ADVANI, S. G. & REINHARDT, A. 2001 Investigation of fiber motion near solid boundaries in simple shear flow. *Rheologica acta* **40** (3), 296–306.
- NI, R., KRAMEL, S., OUELLETTE, N. T & VOTH, G. A. 2015 Measurements of the coupling between the tumbling of rods and the velocity gradient tensor in turbulence. *J. Fluid Mech.* **766**, 202–225.
- PASCHKEWITZ, J. S., DUBIEF, Y., DIMITROPOULOS, C. D., SHAQFEH, E. S. G. & MOIN, P. 2004 Numerical simulation of turbulent drag reduction using rigid fibres. *J. Fluid Mech.* **518**, 281–317.
- QI, D. & LUO, L.S. 2003 Rotational and orientational behaviour of three-dimensional spheroidal particles in couette flows. *J. Fluid Mech.* **477**, 201–213.
- QUILEZ, I. 2016 Cylinder - bounding box. <https://iquilezles.org/articles/diskbbox>.
- ROSÉN, T., EINARSSON, J., NORDMARK, A., AIDUN, C. K., LUNDELL, F. & MEHLIG, B. 2015 Numerical analysis of the angular motion of a neutrally buoyant spheroid in shear flow at small reynolds numbers. *Phys. Rev. E* **92** (6), 063022.

- ROSS, P. S., CHASTAIN, S., VASSILENKO, E., ETEMADIFAR, A., ZIMMERMANN, S., QUESNEL, S.A., EERT, J., SOLOMON, E., PATANKAR, S., POSACKA, A. M. & WILLIAMS, B. 2021 Pervasive distribution of polyester fibres in the arctic ocean is driven by atlantic inputs. *Nature comm.* **12** (1), 1–9.
- SAFFMAN, P. G. 1956 On the motion of small spheroidal particles in a viscous liquid. *J. Fluid Mech.* **1** (5), 540–553.
- SHEIKH, M. Z., GUSTAVSSON, K., LOPEZ, D., LÉVÊQUE, E., MEHLIG, B., PUMIR, A. & NASO, A. 2020 Importance of fluid inertia for the orientation of spheroids settling in turbulent flow. *J. Fluid Mech.* **886**, A9.
- STOVER, C. A. & COHEN, C. 1990 The motion of rodlike particles in the pressure-driven flow between two flat plates. *Rheologica Acta* **29** (3), 192–203.
- SUBRAMANIAN, G. & KOCH, D. L. 2005 Inertial effects on fibre motion in simple shear flow. *J. Fluid Mech.* **535**, 383–414.
- SUBRAMANIAN, G. & KOCH, D. L. 2006 Inertial effects on the orientation of nearly spherical particles in simple shear flow. *J. Fluid Mech.* **557**, 257–296.
- TAYLOR, G. I. 1923 The motion of ellipsoidal particles immersed in a viscous fluid. *Proc. R. Soc. Lond. A* **103** (720), 58–61.
- TREVELYAN, B. J. & MASON, S. G. 1951 Particle motions in sheared suspensions. i. rotations. *J. Colloid Sci.* **6** (4), 354–367.
- VOTH, G. A. & SOLDATI, A. 2017 Anisotropic particles in turbulence. *Annu. Rev. Fluid Mech.* **49** (1), 249–276.
- WANG, Z., XU, C.-X. & ZHAO, L. 2021 Turbulence modulations and drag reduction by inertialess spheroids in turbulent channel flow. *Phys. Fluids* **33** (12), 123313.
- ZETTNER, C. M. & YODA, M. 2001 Moderate-aspect-ratio elliptical cylinders in simple shear with inertia. *J. Fluid Mech.* **442**, 241–266.
- ZHAO, L. & ANDERSSON, H. I. 2016 Why spheroids orient preferentially in near-wall turbulence. *J. Fluid Mech.* **807**, 221–234.